Bio-Design and Manufacturing (2026) 9:579–598
https://doi.org/10.1631/bdm.2500283

RESEARCH ARTICLE

Design and manufacturing of structurally variant nanocarriers for boosting localized chemotherapy against melanoma

Timofey E. Karpov[1] · Anna Rogova[1] · Yulia A. Tishchenko[1] · Irina A. Gorbunova[1,2] · Radmila R. Sergeeva[1] · Sofya V. Faizullina[1] · Thanh Son Cam[3] · Konstantin Chebyshev[4] · Anastasia S. Khapugina[5] · Eugenia J. Platonova[5] · Ivan N. Gaponenko[5] · Alena I. Shakirova[5] · Sergei A. Shipilovskikh[1,2] · Alexander S. Timin[1]

Received: 30 May 2025 / Accepted: 23 December 2025 / Published online: 18 May 2026

Abstract

Nanomedicine has enormous potential in the diagnosis and treatment of malignant neoplasms. However, the clinical translation of various nanoparticles (NPs) as drug delivery systems (DDSs) for tumor therapy remains poor. The main bottleneck is the limited database on the correlation between the design of NPs with unique physicochemical features and their therapeutic efficiency. In this study, we aim to design and investigate structurally variant nanocarriers composed of polylactide (PLA), silicon dioxide (SiO_2), calcium carbonate ($CaCO_3$), and barium carbonate ($BaCO_3$) to reveal the relationship between their physicochemical features and therapeutic effectiveness against melanoma in vitro and in vivo. Specifically, we (1) examined their morphology, size, and structural characteristics; (2) evaluated colloidal stability; (3) verified the drug-loading and release efficiency of a 2-aminothiophene scaffold (2AmT); (4) investigated cellular uptake and tumor spheroid penetration efficiency; (5) analyzed in vivo biodistribution; and (6) estimated therapeutic efficiency. The main characteristics of inorganic and organic NPs were collected and compared systematically. Considering the advantages and drawbacks of each NP type, the following tumor growth inhibition against melanoma was observed: $CaCO_3$ (87.9%–93.4% for 0.4 g/kg of 2AmT)>SiO_2 (75.6%–93.2% for 0.4 g/kg of 2AmT)>PLA (80.3%–88.2% for 0.4 g/kg of 2AmT)>$BaCO_3$ (58.8%–83.7% for 0.4 g/kg of 2AmT). Thus, this study contributes to the development of fundamental nanomedicine and accelerates the clinical translation of nanocarriers for effective melanoma therapy.

✉ Timofey E. Karpov
karpov_te@spbstu.ru

✉ Sergei A. Shipilovskikh
s.shipilovskikh@mail.ru
shipilovskikh@itmo.ru

✉ Alexander S. Timin
a_timin@mail.ru
timin_as@spbstu.ru

[1] Institute of Biomedical Systems and Biotechnology, Peter the Great St. Petersburg Polytechnic University, St. Petersburg 195251, Russian Federation

[2] International and Educational Center for Physics of Nanostructures, ITMO University, St. Petersburg 191002, Russian Federation

[3] Institute of Fundamental and Applied Sciences, Duy Tan University, Ho Chi Minh City 70000, Vietnam

[4] Faculty of Chemistry, North-Caucasus Federal University, Stavropol 355017, Russian Federation

[5] RM Gorbacheva Research Institute of Pediatric Oncology, Hematology and Transplantation, Pavlov University, St. Petersburg 197022, Russian Federation

Graphical abstract

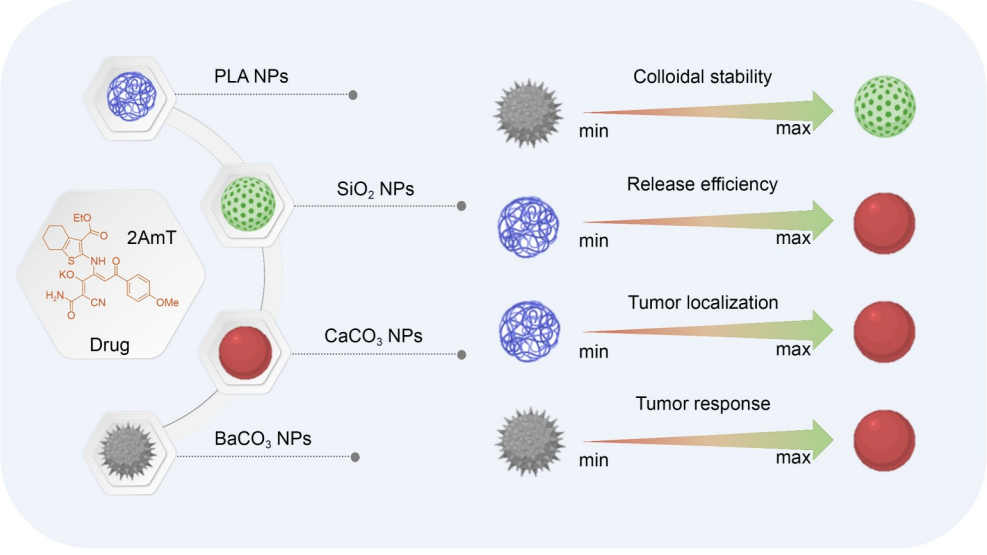

Keywords Inorganic and organic nanoparticles · Physicochemical features · Drug loading and release · Melanoma · Chemotherapy · Clinical translation

1 Introduction

Cancer nanomedicine is a field of medicine focusing on the use of nanomaterials, especially nanoparticles (NPs), for oncological disease prevention, monitoring, and intervention through novel modalities in imaging, diagnosis, and treatment [1, 2]. Currently, many types of NPs have been designed and are considered drug delivery systems (DDSs) to improve the pharmacokinetic properties of individual antitumor drugs [3–6]. The main advantages of NPs as DDSs include tunable morphology, variable size, multiple drug-loading capacity, controllable drug release, and enhanced pharmacokinetics. The controllable and prolonged release of antitumor drugs enables the achievement of high therapeutic efficacy while simultaneously reducing the toxic profile associated with the systemic administration [7–10]. DDSs have demonstrated enormous potential in overcoming the limitations of individual antitumor drugs [11]. Despite the promising features of NPs, only around 21 DDSs have been implemented in clinical practice for cancer therapy [12]. Unfortunately, in most cases, the developed NPs as DDSs have failed clinical trials; only about 14% of the designed NPs have demonstrated potential therapeutic effects [13]. Thus, clinically translating NPs for diagnosing and treating various tumors is highly challenging.

The poor clinical translation of NPs may be attributed to a lack of comprehensive understanding of the fundamental interactions between NPs and biological systems in vitro and in vivo [14]. Many scientists have raised key questions regarding how the physicochemical properties of NPs influence their biodistribution. For instance, what is the mechanism by which NPs travel? How can the physicochemical features affect NP fate [1]? Significant progress in this field has been achieved through investigations of physicochemical-dependent transport of various nanocarriers within tumors [15–17]. Recently, mechanisms of NP delivery into solid tumors have been proposed and defined, which are crucial for the clinical translation of cancer nanomedicine and identifying how NPs should be engineered for medical applications [18]. However, the relationship between the design of nanocarriers with unique physicochemical features and their therapeutic efficiency against solid tumors remains poorly investigated [3, 17, 19]. To date, few studies have described the design of the physicochemical parameters of NPs specifically targeting cancer therapy [20]. Additionally, there are problems associated with batch-to-batch nonuniformity, long-term stability, complexity in processing methods, and discrepancies between academic progress and regulatory bodies [21]. Therefore, before initiating clinical trials, thorough investigations are required to identify the physicochemical-dependent therapeutic properties of NPs.

Here, we specifically focus on the design and manufacturing of structurally variant nanocarriers with unique physicochemical features applied in biomedical engineering for localized chemotherapy. Understanding the relationship between the physicochemical features of NPs and their

therapeutic effectiveness can help in the design and production of novel dosage forms with robust safety and efficacy relative to current clinical standards. For this purpose, four types of NPs were considered, consisting of polylactide (PLA), silicon dioxide (SiO_2), calcium carbonate ($CaCO_3$), and barium carbonate ($BaCO_3$). To demonstrate therapeutic efficacy, these NPs were loaded with an antitumor drug based on a 2-aminothiophene scaffold (2AmT). The selection of PLA, SiO_2, $CaCO_3$, and $BaCO_3$ NPs was based on their biocompatibility, biodegradability, sustainable delivery capability, and controlled release kinetics [22–24]. Moreover, these nanocarriers have been approved for human use, and some have successfully passed clinical trials. For instance, SiO_2 NPs are currently under clinical investigation for real-time image-guided intraoperative mapping of nodal metastases (NCT02106598). $CaCO_3$ particles have completed Phase 1 trials for colon cancer prevention (NCT02647671). PLA NPs have been approved for human vaccine application as nanoformulations for drug delivery and controlled drug release [25]. In addition, barium-based materials are clinically approved as contrast agents in radiography [26]. Melanoma was selected as a highly lethal and aggressive cancer type [7, 27]. This tumor has high rates of recurrence, progression, and metastasis [28]. The step-by-step procedures included: (1) synthesis of PLA, SiO_2, $CaCO_3$, and $BaCO_3$ NPs with similar sizes, (2) analysis of the drug-loading and release efficiency of 2AmT, (3) investigation of cellular interactions in two-dimensional (2D) and three-dimensional (3D) cell cultures, (4) in vivo biodistribution analysis, and (5) estimation of therapeutic effectiveness against melanoma in localized chemotherapy. The overall methodology of the current study is illustrated in Fig. 1.

2 Materials and methods

2.1 Materials

Detailed information on the chemicals used to synthesize 2AmT, PLA, SiO_2, $CaCO_3$, and $BaCO_3$ NPs is summarized

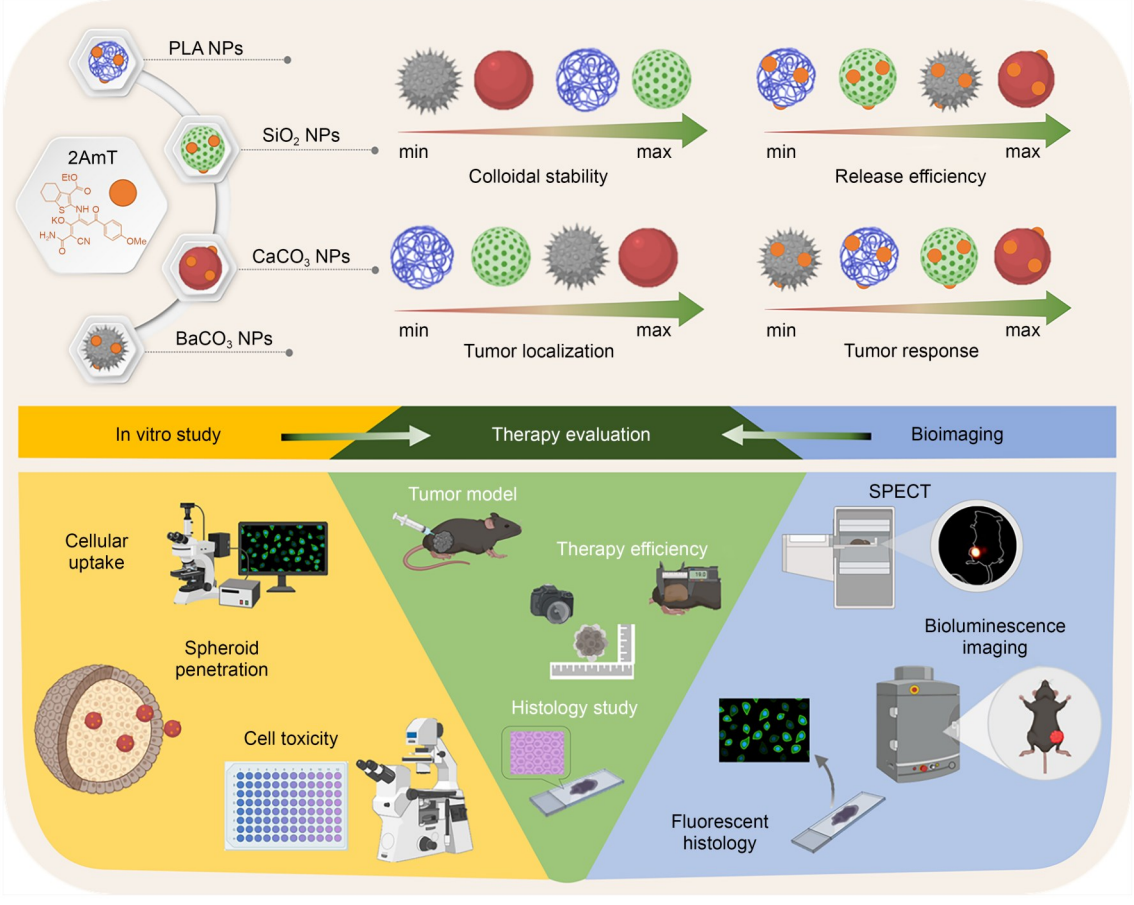

Fig. 1 Overall methodology of the current study. It includes the synthesis of four types of DDSs—PLA, SiO_2, $CaCO_3$, and $BaCO_3$ NPs—with the drug loading of 2AmT. The in vitro studies consisted of cellular uptake, tumor spheroid penetration, and cell viability. The in vivo studies were divided into (1) biodistribution analyses (fluorescent bioimaging, single-photon emission computed tomography (SPECT), and fluorescent histology) and (2) analyses of therapeutic effectiveness after localized chemotherapy, including the formation of a tumor model, evaluation of tumor size, and histological examination of the tumor and the primary organs

in Sect. S1 (supplementary information). Additionally, the materials and consumables for the in vitro and in vivo experiments are presented in Sect. S1 (supplementary information).

2.2 Synthesis of the antitumor drug (2AmT)

The antitumor drug (2AmT) was selected for cargo loading because of its therapeutic effect against melanoma in vitro and in vivo [29]. The full International Union of Pure and Applied Chemistry (IUPAC) name is potassium 1-amino-2-cyano-4-((3-(ethoxycarbonyl)-4,5,6,7-tetrahydrobenzo[*b*]thiophen-2-yl)amino)-6-(4-methoxyphenyl)-1,6-dioxohexa-2,4-dien-3-olate. 2AmT synthesis is illustrated in Fig. S1 (supplementary information). The synthesized antitumor drug was characterized with ^{1}H nuclear magnetic resonance (NMR) and ^{13}C NMR spectroscopy (Figs. S2 and S3 in the supplementary information). The detailed synthesis is described in Sect. S2.1 (supplementary information).

2.3 NPs synthesis

2.3.1 PLA NPs

The synthesis of PLA NPs has been accomplished using a modified nanoprecipitation protocol [30]. In this context, a solution of PLA in dichloromethane was mixed with another solution containing acetone/ethanol in a volume ratio of 4:1. The organic solution was then added to Milli-Q water under constant magnetic stirring. The evaporation of organic solvents using prolonged magnetic stirring has been utilized to obtain a stable aqueous suspension of PLA NPs. The procedural details are provided in Sect. S2.2.1 (supplementary information).

2.3.2 SiO_2 NPs

SiO_2 NPs were synthesized by the sol–gel technique. Specifically, ethanol and Milli-Q water were mixed, and then tetraethyl orthosilicate and ammonium hydroxide solution (NH_4OH) were slowly added to the mixture under stirring conditions. The resulting solution was vigorously agitated for 2 h. The SiO_2 NP solution was then centrifuged at 12 000 r/min for 5 min and washed several times with ethanol and Milli-Q water. The detailed procedures are shown in Sect. S2.2.2 (supplementary information).

2.3.3 $CaCO_3$ NPs

$CaCO_3$ NPs were synthesized using the co-precipitation technique [31, 32]. Briefly, 0.1 mol/L calcium chloride ($CaCl_2$) solution was mixed with 3.0 mg/mL polyacrylic acid (PAA) solution and stirred for 1 h. Then, 0.1 mol/L sodium carbonate (Na_2CO_3) solution was added, and the solution was stirred for 1 h. The resulting suspension of $CaCO_3$ NPs was centrifuged at 13 000 r/min for 3 min and washed with ethanol, and the pellets were collected for further analysis. The details are provided in Sect. S2.2.3 (supplementary information).

2.3.4 $BaCO_3$ NPs

$BaCO_3$ NPs were synthesized by mixing PAA, Na_2CO_3, and $BaCl_2{\cdot}2H_2O$ in ethylene glycol solution (EG:H_2O volume ratio=2.5: 1) at pH 3–5, followed by dropwise addition of PAA/Na_2CO_3 to PAA/$BaCl_2$ and stirring for 1 h. The resulting mixture was washed several times with ethanol via centrifugation and resuspended for further use. The details are provided in Sect. S2.2.4 (supplementary information).

2.3.5 2AmT_NPs

The following procedure was used to prepare 2AmT-loaded NPs (2AmT_NPs). First, polymer coatings were added to the PLA, SiO_2, $CaCO_3$, and $BaCO_3$ NPs using the layer-by-layer method with positively charged polyethylenimine (PEI). Then, the PEI-coated NPs were incubated with 2AmT in dimethyl sulfoxide (DMSO) for 1 h. The resulting 2AmT_NPs were washed several times with Milli-Q water to remove the unbound 2AmT. The details are presented in Sect. S2.3 (supplementary information).

2.3.6 Cyanine 5-labeled NPs (Cy5_NPs)

Cy5_NPs were prepared by conjugating Cy5 dye with bovine serum albumin (BSA) in phosphate-buffered saline (PBS) at 4 °C for 24 h, followed by dialysis to remove unreacted Cy5 dye. Then, the adsorption of Cy5-BSA onto PLA, SiO_2, $CaCO_3$, and $BaCO_3$ NPs was performed, followed by centrifugation washing, during which the supernatants were monitored to ensure complete removal of free Cy5. The details are presented in Sect. S2.4 (supplementary information).

2.4 NPs characterization

2.4.1 Morphological and size characterization

The morphological characteristics and size distribution of the synthesized NPs were characterized using electron microscopy techniques. The scanning electron microscopy (SEM) was conducted using a Quanta 200 FEI microscope (FEI Company, the Netherlands), equipped with energy-dispersive X-ray spectroscopy (EDX) for elemental composition. The high-resolution images of nanoparticles were obtained using transmission electron microscopy (TEM) with a JEOL JEM-1011 electron microscope (JEOL Ltd., Japan). Furthermore, the hydrodynamic diameter (D_h) was determined using dynamic light scattering (DLS) with a BK

Winner803 DLS Nano Particle Analyzer (Jinan Winner Particle Instrument Stock Co., Ltd., China).

2.4.2 Structural characterization

Fourier transform infrared spectroscopy (FTIR, Tensor 27, Bruker, Germany) was used to characterize the functional groups of the synthesized NPs. For each spectrum, 50 scans between 4000 and 400 cm^{-1} were recorded in attenuated total reflection mode. The nanoscale structure of the NPs was confirmed using powder X-ray diffraction (PXRD) analysis (XRD-7000, Shimadzu, Japan).

2.4.3 Surface characterization

Surface analysis (specific surface area and pore size) was determined by measuring the low-temperature (77 K) adsorption–desorption isotherms of nitrogen (N_2) on a NOVA 1200e Surface Area & Pore Size Analyzer (Quantachrome Instruments, USA). Pore size distributions were analyzed using the Barrett–Joyner–Halenda (BJH) method applied to the desorption branch of the isotherm. The surface charge was measured using a Zetasizer Nano ZS90 (Malvern Instruments, UK) to determine the zeta potential. The details are presented in Sect. S3.6 and S3.7 (supplementary information).

2.5 Colloidal stability of the developed NPs

The colloidal stability of the PLA, SiO_2, $CaCO_3$, and $BaCO_3$ NPs was investigated over 18 d by measuring the D_h value at specific time points. Two aqueous media at pH 3.5 and pH 7.0 were used for colloidal stability analysis: (1) 0.9% (mass fraction) sodium chloride (NaCl) solution and (2) 0.1% (mass fraction) BSA solution. More detailed information is presented in Sect. S4 (supplementary information).

2.6 Drug-loading and release efficiency

2.6.1 Drug loading

A NanoPhotometer C40-Touch (Implen, Germany) was employed to estimate the loading efficiency of 2AmT (10 mg) into the PLA, SiO_2, $CaCO_3$, and $BaCO_3$ NPs (30 mg). The absorbance spectra of the supernatants collected after each washing step were recorded at 343 nm. Calibration curves showing the relationship between absorbance and 2AmT concentration were prepared in various biological media (0.9% NaCl and 0.1% BSA) at pH 3.5 and 7.0. More detailed information is presented in Sect. S5.1 (supplementary information).

2.6.2 Drug-release analysis

The drug release profiles of 2AmT_PLA, 2AmT_SiO_2, 2AmT_$CaCO_3$, and 2AmT_$BaCO_3$ were investigated in 0.9% NaCl and BSA at pH 3.5 and 7.0. The absorbance spectra of the supernatants were measured. After removing the supernatants, the 2AmT_PLA, 2AmT_SiO_2, 2AmT_$CaCO_3$, and 2AmT_$BaCO_3$ NPs were resuspended in fresh solutions (0.9% NaCl and BSA) and shaken on a thermoshaker (TS-100C, Biosan, Latvia). The amount of released 2AmT was indirectly calculated using the calibration curves. More detailed information is provided in Sect. S5.2 (supplementary information).

2.7 Cell experiments

2.7.1 2D cellular uptake

Cellular uptake of the PLA, SiO_2, $CaCO_3$, and $BaCO_3$ NPs was investigated in B16-F10 melanoma cells using a confocal laser scanning microscope (CLSM; TCS SP8, Leica Microsystems, Germany). For CLSM visualization, the cytoskeletons of the cells were stained with phalloidin conjugated with fluorescein isothiocyanate (FITC), and the nuclei of the cells were stained with propidium iodide (PI). The NPs were modified with Cy5 fluorescent dye. Detailed information on the cell cultivation and incubation with NPs is described in Sect. S6.2 (supplementary information).

2.7.2 Flow cytometry analysis

Flow cytometry analysis was conducted to investigate the association of B16-F10 melanoma cells with the Cy5-labeled PLA, SiO_2, $CaCO_3$, and $BaCO_3$ NPs. Cy5-labeled particles were added to the cells at concentrations of 2, 4, and 8 mg/mL. The measurements were performed at 650 nm with a long-pass filter for Cy5 and analyzed using flow cytometry (FACS Aria, BD, USA).

2.7.3 Three-dimensional tumor spheroid penetration

The tumor spheroids were formed using the hanging drop method [33]. The formed tumor spheroids were incubated with Cy5-modified NPs (4 mg/mL). CLSM imaging was used to examine the ability of NPs to penetrate the tumor spheroids. For CLSM visualization, tumor spheroids were fluorescently stained with PI. Then, 3D stack images were taken with a TCS SP8 (Leica Microsystems). More detailed information is described in Sect. S6.3 (supplementary information).

2.7.4 Cell viability

Cell viability of B16-F10 melanoma cells exposed to 2AmT_NPs was evaluated using the Alamar Blue assay. B16-F10 cells were initially seeded into 96-well plates to establish a standardized monolayer culture prior to NP incubation. Then, 2AmT_NPs were added to cells at different amounts (0.2, 0.5, 0.9, 1.9, 3.7, 7.5, 15.0, and 30.0 μmol/L 2AmT). After 24 h of incubation, the cell medium was changed to Alamar Blue solution (10% volume fraction) and incubated for 4 h. The cell viability was estimated

using a standard protocol [29]. The morphology of B16-F10 cells was evaluated using the optical microscope NIB-FL (LOMO-MA, Russian Federation). Further comprehensive details are provided in Sect. S6.5 (supplementary information).

2.7.5 Hemolysis assay

The NP impact on the viability of human red blood cells (RBCs) was examined using a standard hemolysis assay [34]. RBCs were isolated from blood plasma via Ficoll density gradient centrifugation and subsequently washed multiple times to ensure purity. NPs were added to the RBC solution at different concentrations (0.25–10.00 mg/mL). The released hemoglobin in the supernatants was quantified by measuring the absorbance at 540 nm with a spectrophotometer. Further comprehensive details are provided in Sect. S7 (supplementary information).

2.8 In vivo biodistribution analysis

C57BL/6 mice were used as a B16-F10 melanoma tumor model. More details on the animals and tumor models are presented in Sect. S8 and S9 (supplementary information). The mice with tumors were used as subjects for the following in vivo experiments: (1) biodistribution (fluorescent bioimaging, single-photon emission computed tomography (SPECT), and direct radiometry) and (2) in vivo treatment (tumor size measurement, body weight measurement, and histological analysis). All animal procedures were performed in accordance with the Guidelines for Care and Use of Laboratory Animals of Peter the Great St. Petersburg Polytechnic University and approved by the local Animal Ethics Committee of the Institute of Biomedical Systems and Biotechnology of Peter the Great St. Petersburg Polytechnic University. The composition of the local Animal Ethics Committee was approved by Order No. 21 dated 26 February 2020. The ethical approval order was No. 01, dated 3 February 2025.

2.8.1 Fluorescent bioimaging

The Cy5-labeled PLA, SiO_2, $CaCO_3$, and $BaCO_3$ NPs were injected into the tumors of tumor-bearing mice. The mice were sacrificed, and the tumors were extracted. The Fluor i in vivo NeuroScience system was used for fluorescent bioimaging. The fluorescent signals for the tumors were measured as intensity units (intensity/min/gain). More detailed information is presented in Sect. S11.1 (supplementary information).

2.8.2 Single-photon emission computed tomography

SPECT was used to analyze the distribution of the radiolabeled NPs. The PLA, SiO_2, $CaCO_3$, and $BaCO_3$ NPs were modified with ^{99m}Tc diagnostic isotopes. Then, the radiolabeled nanocarriers were injected into tumor-bearing mice. Planar SPECT imaging was performed on a Discovery NM 630 (GE Healthcare, USA) using a low-energy general-purpose high-resolution collimator (GE Healthcare). Further comprehensive details are provided in Sect. S11.2 (supplementary information).

2.8.3 Direct radiometry

The mice with injected radiolabeled NPs were sacrificed, and the major organs (heart, lungs, liver, spleen, and kidneys) and tumors were examined using a TRIATHLER portable spectrometric radiometer (Hidex Oy, Finland). The radiolabeling signals in the organs were calculated as a percentage of the injected dose per gram of tissue (ID/g (%)). Further comprehensive details are provided in Sect. S11.3 (supplementary information).

2.8.4 Fluorescent histological analysis of tumor tissues

Tumor tissues were extracted and prepared for fluorescent histological analysis. TCS SP8 (Leica Microsystems) was used to analyze histological sections of the tumors. More detailed information is presented in Sect. S12.2 (supplementary information).

2.9 Localized chemotherapy

In vivo therapy was initiated when the solid tumor volume reached approximately (0.05 ± 0.01) cm^3. The following groups were considered: Control (PBS); 2AmT (0.2 and 0.4 g/kg); 2AmT_PLA (0.2 and 0.4 g/kg); 2AmT_SiO_2 (0.2 and 0.4 g/kg); 2AmT_$CaCO_3$ (0.2 and 0.4 g/kg); and 2AmT_$BaCO_3$ (0.2 and 0.4 g/kg). To estimate the efficacy of the therapy, three methods were used: (1) tumor size measurement, (2) body weight measurement, and (3) histological analysis. More detailed information is presented in Sect. S13.1 (supplementary information).

2.9.1 Tumor size measurement

Subcutaneous tumors were measured in manually restrained awake mice using digital calipers (accuracy: 0.01 cm). The length (largest diameter) and width (perpendicular short diameter) of the tumor were recorded during therapy, starting when the tumor size reached (0.05 ± 0.01) cm^3 until the end of the study. The tumor volume was calculated using a modified ellipsoid formula: $\text{volume}=\text{length}\times\text{width}^2\times1/2$. This standard formula provides a reliable estimate of tumor burden and was used to monitor progression and treatment efficacy.

2.9.2 Body weight measurement

The weights of the mice were measured using a standard analytical scale (SP402, Ohaus, USA). Measurements were taken on 1, 2, 4, 6, and 8 d after the start of the treatment.

2.9.3 Histological analysis

Tissues from the primary organs (heart, lungs, liver, spleen, and kidneys) and tumors were isolated and prepared for hematoxylin and eosin (H&E) staining using an HM 340E rotary microtome (Thermo Scientific). The obtained histological H&E-stained slices were visualized with a Panoramic MIDI II Digital Scanner (3DHISTECH, Hungary) and CLSM TCS SP8 (Leica Microsystems). Further comprehensive details are provided in Sect. S13.2 (supplementary information).

2.10 Statistics

Statistical evaluations were conducted using OriginLab software (OriginLab Corporation, Northampton, MA, USA). Data are reported as mean±standard deviation or mean±standard error of the mean. Experimental results underwent one-way analysis of variance (ANOVA), followed by Tukey's post hoc test for intergroup comparisons. Statistical significance was established at a threshold of $p<0.05$.

3 Results and discussion

3.1 Morphological and size characterization

The SEM and TEM images of the PLA, SiO_2, $CaCO_3$, and $BaCO_3$ NPs showed spherical morphology with average sizes of approximately 130 nm for PLA, 90 nm for SiO_2, 120 nm for $CaCO_3$, and 140 nm for $BaCO_3$ (Figs. 2b and 2c). Additional representative images of the PLA, SiO_2, $CaCO_3$, and $BaCO_3$ NPs are presented in Figs. S4–S7 (supplementary information). The PLA and SiO_2 NPs exhibited solid spherical nanospheres. $CaCO_3$ NPs demonstrated minimal surface irregularities. $BaCO_3$ NPs showed surface bulges. Figure 2d shows the size distribution of NPs. The EDX spectra confirmed the presence of necessary elements like Ca, Ba, Si, C, and O (Fig. S8 in the supplementary information). The average hydrodynamic diameters (D_h) were around 235–255 nm for all NP types (Fig. 2e). The average D_h was 244.09 nm for PLA NPs, 254.90 nm for SiO_2 NPs, 235.42 nm for $CaCO_3$ NPs, and 254.19 nm for $BaCO_3$ NPs. The insets in Fig. 2e, show digital photos of white, homogeneous suspensions of the NPs without any visible aggregation.

3.2 Structural, colloidal stability, and surface characterization

FTIR spectroscopy confirmed the chemical composition of the developed NPs (Fig. 3a). For the $BaCO_3$ and $CaCO_3$ NPs, the characteristic peaks at 1537 cm^{-1} and 1410–1400 cm^{-1} were attributed to the asymmetric stretching vibration of C=O in the carbonate group (CO_3^{2-}) (ν_3 mode), the peak at 860 cm^{-1} was attributed to the out-of-plane bending of CO_3^{2-} (ν_2 mode) [35], and the broad band at 3400–3000 cm^{-1} was assigned to O–H stretching of adsorbed water. For the PLA NPs, multiple peaks at 2990 and 2940 cm^{-1} were associated with C–H stretching vibrations of the methyl (–CH_3) group [36] and in the PLA chain (e.g., approximately 2990 cm^{-1} for asymmetric CH_3 stretching, 2940 cm^{-1} for symmetric –CH_3 stretching). The absorption peak at 1750 cm^{-1} was attributed to the C=O stretching vibration of the ester carbonyl group, the peak at 1450 cm^{-1} was associated with –CH_3 bending vibration (asymmetric deformation), the peak at 1380 cm^{-1} was attributed to the –CH_3 bending vibration (symmetric deformation), the peak at 1182 cm^{-1} represented the C–O–C stretching of the ester linkage, and the peak at 1080 cm^{-1} showed C–O stretching of the polymer backbone. For the SiO_2 NPs, a strong peak at 1066 cm^{-1} was attributed to asymmetric stretching of Si–O–Si bonds, while a band at 800 cm^{-1} was associated with symmetric stretching of Si–O–Si, a peak at 900 cm^{-1} was attributed to Si–OH stretching, and a peak at 450 cm^{-1} demonstrated Si–O–Si bending vibration. Consistent with the $BaCO_3$ and $CaCO_3$ samples, a similar band for O–H stretching was observed at 3400–3000 cm^{-1} for SiO_2 NPs [37]. All NPs showed amorphous structures as evidenced by PXRD (Fig. S9 in the supplementary information). Furthermore, Fig. 3b shows the colloidal stability of the developed NPs examined in NaCl and BSA solutions over a long period (18 d). Three points (1, 8, and 18 d) are presented in the main paper. The other points (5, 12, and 15 d) and histograms of the D_h distributions for each NP type are provided in Figs. S10–S13 (supplementary information). At a neutral pH, the NPs displayed high stability with minimal changes in D_h. However, some fluctuations in the average D_h were observed at pH 3.5. In general, the average D_h values were in the range of 150–350 nm. Additionally, we performed zeta-potential analysis of NPs on Days 1 and 18 in deionized water to evaluate their intrinsic electrostatic stability. The zeta potentials of the NPs were: ζ(PLA, 1 d)=(−11.80±0.67) mV, ζ(PLA, 18 d)=(−16.10±0.55) mV, ζ(SiO_2, 1 d)=(−21.58±0.75) mV, ζ(SiO_2, 18 d)=(−27.88±1.31) mV, ζ($CaCO_3$, 1 d)=(−8.06±0.17) mV, ζ($CaCO_3$, 18 d)=(−11.10±0.28) mV, ζ($BaCO_3$, 1 d)= (−5.58±0.36) mV, and ζ($BaCO_3$, 18 d) = (−10.19±0.75) mV. These results are consistent with previous values [38−43]. The data were summarized in Table 1.

The specific surface area and porosity of the developed NPs were examined with nitrogen adsorption–desorption isotherms and BJH pore size distribution analysis. The pore-filling process is depicted in Fig. 3c. The obtained isotherms revealed differences in adsorption behavior, reflecting the structural diversity of the NPs (Fig. 3d1). It should be noted that the PLA NPs were not analyzed with Brunauer−Emmett−Teller (BET) or BJH due to their limited thermal stability

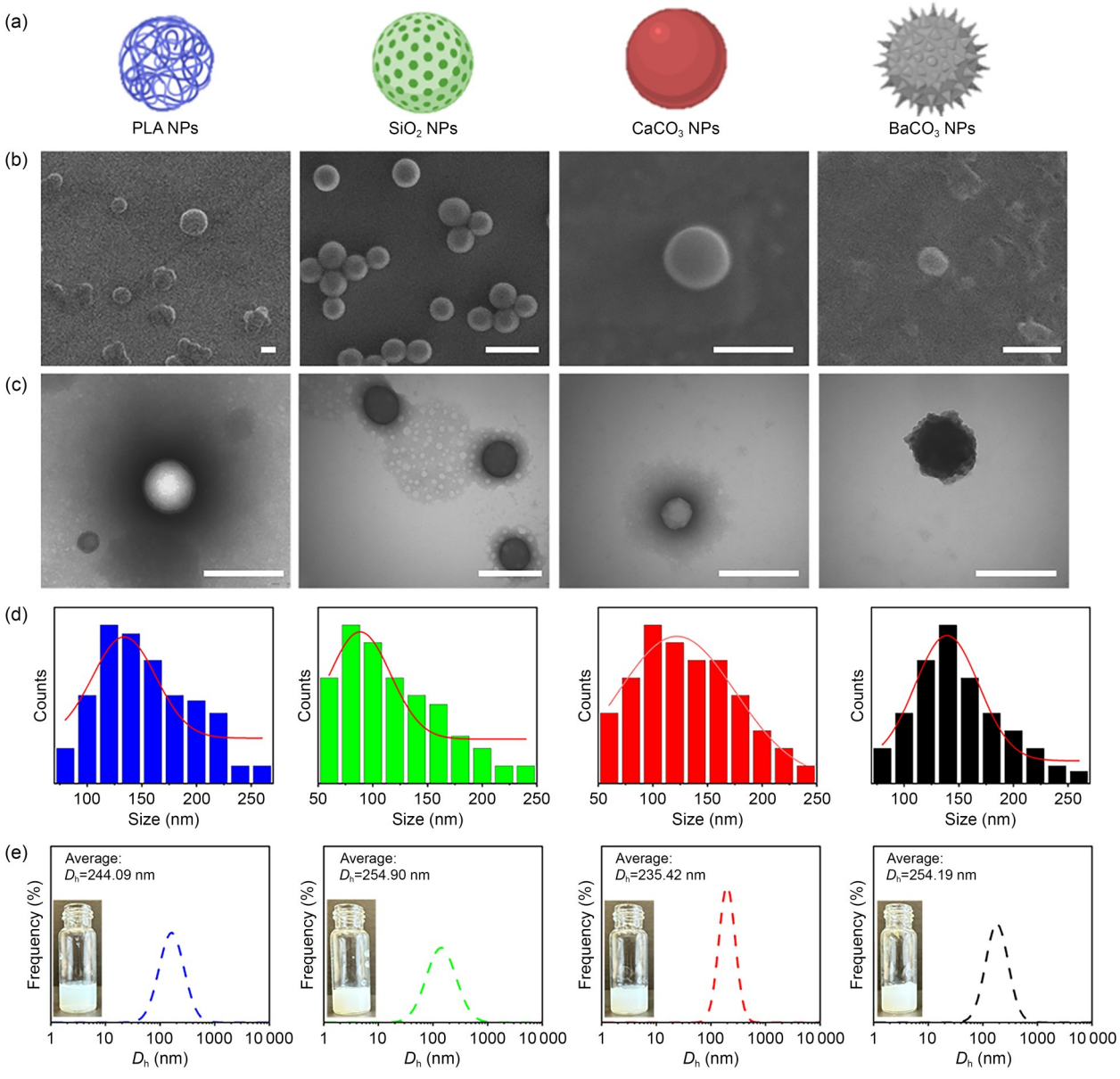

Fig. 2 Characterization of the PLA, SiO_2, $CaCO_3$, and $BaCO_3$ NPs. (a) Schematic illustration of each nanoparticle type. (b) SEM images of PLA, SiO_2, $CaCO_3$, and $BaCO_3$ NPs. Scale bars: 200 nm. (c) TEM images of PLA, SiO_2, $CaCO_3$, and $BaCO_3$ NPs. Scale bars: 200 nm. (d) Size distribution for PLA, SiO_2, $CaCO_3$, and $BaCO_3$ NPs. (e) Hydrodynamic diameters (D_h) for PLA, SiO_2, $CaCO_3$, and $BaCO_3$ NPs measured in 0.9% NaCl solution (pH 7.0)

during sample preparation (below the degassing temperature, which was approximately 300 °C) [44]. The SiO_2 NPs exhibited an isotherm with a more pronounced stepwise uptake, reaching 47 cm^3/g, and a hysteresis loop [45]. The pore size distribution was centered at 3.2 nm (Fig. 3d2, green curve). The isotherm of the $CaCO_3$ NPs exhibited a type II profile. An average pore diameter of 3.5 nm was observed (Fig. 3d2, red curve). The $BaCO_3$ NPs showed a type III isotherm. The BJH analysis revealed a pore size distribution peaking at <2 nm (Fig. 3d2, black curve). The calculated BET surface area and pore size for the developed NPs are summarized in Table 2.

A detailed discussion on the colloidal stability, BET surface area, and pore size of the NPs is considered further in Sect. 3.7.

3.3 Drug-loading and release efficiency of the developed NPs

Drug loading was performed by incubation of PEI-coated NPs in 2AmT solution. The amount of adsorbed 2AmT was estimated using calibration curves (Fig. S14 in the supplementary information) during the washing steps (Fig. 4a). Figure 4b shows digital photos of the 2AmT-loaded NPs

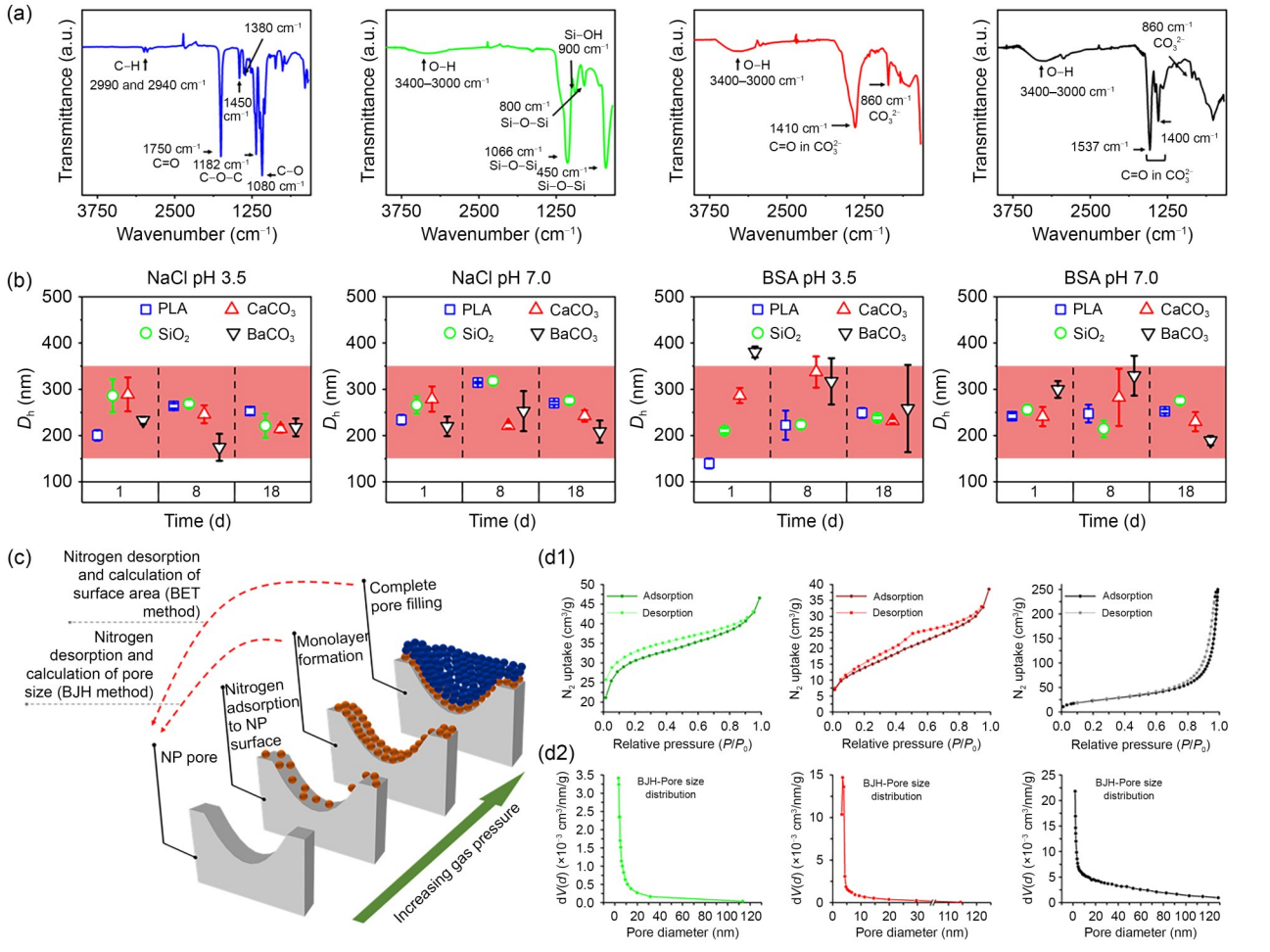

Fig. 3 Structural characterization of PLA (blue), SiO_2 (green), $CaCO_3$ (red), and $BaCO_3$ (black) NPs. (a) FTIR spectra of PLA (blue), SiO_2 (green), $CaCO_3$ (red), and $BaCO_3$ (black) NPs, shown in transmittance mode (arbitrary units, a.u.). (b) Colloidal stability of PLA, SiO_2, $CaCO_3$, and $BaCO_3$ NPs was examined in NaCl and BSA solutions for 18 d. The results are shown as mean±standard deviation (n=3). (c) BET analysis and pore-filling process. (d1, d2) Nitrogen adsorption–desorption isotherms of SiO_2 (green), $CaCO_3$ (red), and $BaCO_3$ (black) NPs with corresponding pore size distribution curves

Table 1 Zeta-potential analysis of the NPs on Days 1 and 18

NP type	Zeta potential at 1 d (mV)	Zeta potential at 18 d (mV)
PLA	−11.80±0.67	−16.10±0.55
SiO_2	−21.58±0.75	−27.88±1.31
$CaCO_3$	−8.06±0.17	−11.10±0.28
$BaCO_3$	−5.58±0.36	−10.19±0.75

Table 2 BET specific surface area analysis with corresponding pore size distribution

NP type	BET surface area (m^2/g)	Average pore size (nm)
PLA	–	–
SiO_2	98.93	3.2
$CaCO_3$	51.05	3.5
$BaCO_3$	84.38	<2

and the corresponding supernatants after each washing step. The drug-loading efficiency was: (66.71±1.99)% for PLA NPs, (74.15±3.74)% for SiO_2 NPs, (75.29±3.56)% for $CaCO_3$ NPs, and (72.71±4.44)% for $BaCO_3$ NPs.

To evaluate the release behavior of 2AmT from the four NPs, they were incubated in two solutions, i.e., 0.9% NaCl and 0.1% BSA at pH 3.5 and 7.0. The neutral pH 7.0 and acidic pH 3.5 were selected to demonstrate the difference in the drug release profiles of 2AmT at various pH values. This was done to maximally verify the pH-responsive mechanism of drug release across all tested NPs. Similar algorithms have been reported in previous works [46, 47]. Figure 4c shows the release profiles of 2AmT among the tested NPs. The cumulative drug release was relatively low; specifically, the maximum values reached (12.68±1.27)% for the 0.9% NaCl solution and (18.88±1.89)% for the 0.1% BSA solution at pH 7.0. In contrast, the NPs exhibited a higher release of 2AmT at pH 3.5. Specifically, in 0.1% BSA solution, $BaCO_3$ and $CaCO_3$ NPs displayed the maximum release of (39.98±2.40)% and (40.11±2.01)%, respectively.

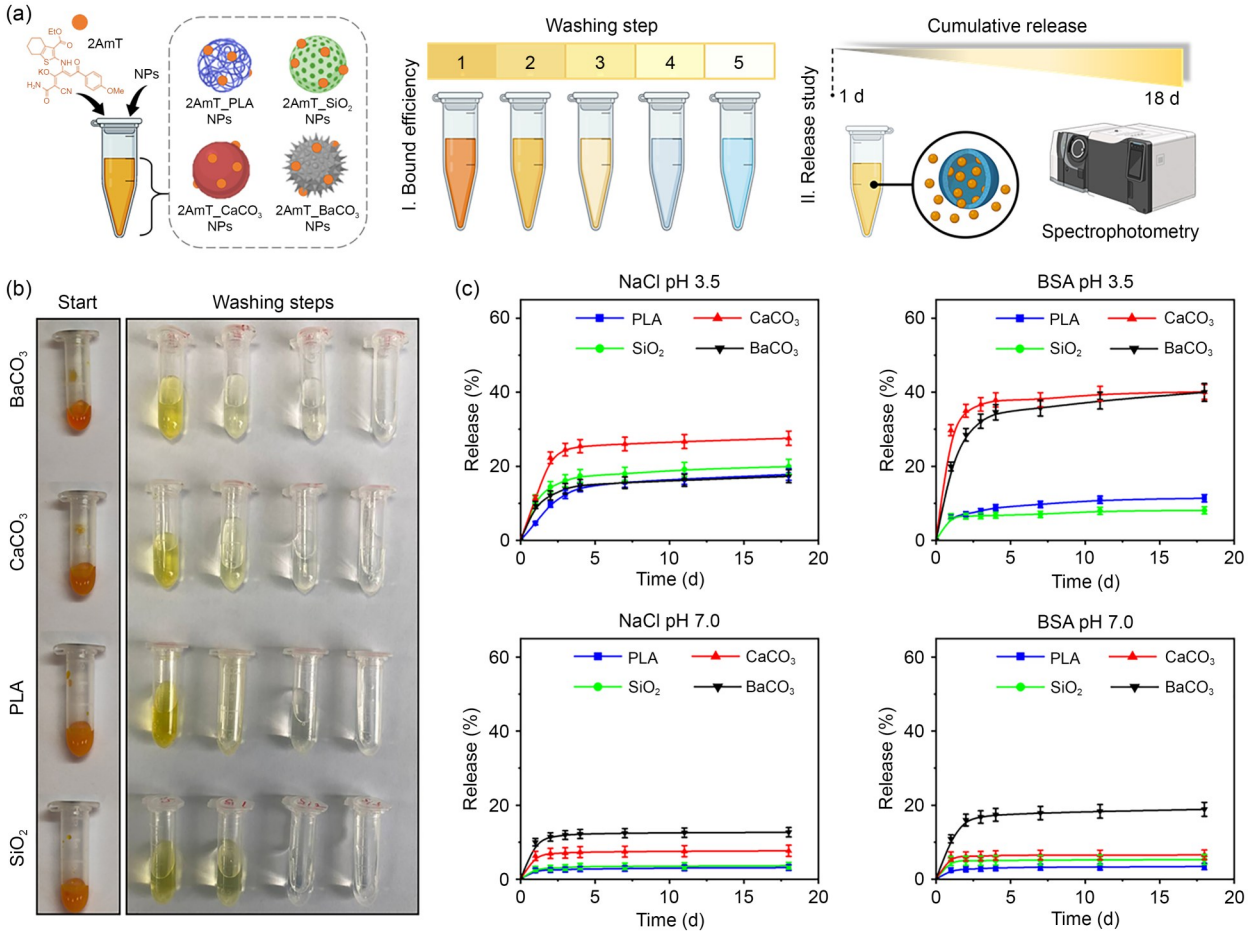

Fig. 4 Drug-loading and release efficiency of 2AmT among PLA, SiO_2, $CaCO_3$, and $BaCO_3$ NPs. (a) Schematic illustration of the drug adsorption process with washing and cumulative release analysis. (b) Representative photos of the 2AmT-loaded PLA, SiO_2, $CaCO_3$, and $BaCO_3$ NPs together with supernatants collected during the washing steps. (c) Time-dependent release profiles of 2AmT from NPs incubated under various conditions: 0.9% NaCl (pH 3.5 and pH 7.0) and 0.1% BSA (pH 3.5 and pH 7.0). The results are shown as mean±standard deviation (n=3)

However, in 0.9% NaCl solution, the highest release was observed for $CaCO_3$ ((27.58±1.93)%), while $BaCO_3$, PLA, and SiO_2 demonstrated lower and relatively similar profiles ranging from approximately 17% to 20%. The enhanced release for carbonate-based NPs (especially in BSA) can be attributed to pH-dependent matrix dissolution, as $BaCO_3$ and $CaCO_3$ are known to partially dissolve in acidic conditions, leading to the degradation of the NP structure [48, 49]. In our case, the presence of BSA further enhanced this process, likely due to weak complexation of divalent cations (Ba^{2+} and Ca^{2+}) and interactions between albumin and the carbonate surface, which prevent surface passivation and promote continuous dissolution [50]. This synergistic effect explains the markedly higher release of 2AmT in the BSA medium compared to NaCl at pH 3.5. Consequently, more complete drug release was achieved as the particles degraded. Otherwise, the PLA and SiO_2 NPs are more stable and retain their structure even under acidic conditions (pH 3.5). In these systems, BSA tends to adsorb on the nanoparticle surface, forming a protein corona [51], limiting 2AmT diffusion and partially binding the released molecules, resulting in a lower apparent release compared with the NaCl medium. Therefore, the drug release from these more stable carriers occurs mainly through electrostatic repulsion between the nanoparticle surface and the adsorbed 2AmT molecules. Altogether, these findings highlight that both the environmental pH and the composition of the surrounding medium (ionic versus protein-containing) affect the cumulative release behavior of 2AmT from NPs.

3.4 Cellular uptake, tumor spheroid penetration, and toxicity

Next, in vitro experiments were performed to investigate the cellular uptake in 2D and 3D cell cultures. The cellular internalization of NPs in B16-F10 cells was examined using CLSM. NPs were conjugated with Cy5 fluorescent dye (Cy5_NPs). The fluorescent labeling is described in Sect. S2.4 (supplementary information). The Cy5-loaded NPs were washed several times by centrifugation (12 000 r/min, 3 min)

to remove unbound Cy5 dye. The purification steps were monitored by visual observation and analysis of supernatant absorption spectra to ensure that the fluorescence truly reflects NP retention and metabolism in tumor tissues (Fig. S15 in the supplementary information). Figure 5a and Fig. S16a (supplementary information) illustrate Cy5_NP internalization. The NPs demonstrated high internalization ability; i.e., the red Cy5 signal was localized throughout the cell cytoplasm. As the NP concentration increased (8 mg/mL), the intensity and localization of the red Cy5 signal increased accordingly. CLSM images collectively demonstrated the concentration-dependent internalization efficiency of the developed NPs. Additionally, the cell–NP association was monitored using flow cytometry. Figure 5b and Fig. S16b (supplementary information) demonstrate the cell–NP associations among the tested NPs. B16-F10 cells provided a high uptake efficiency for the Cy5-labeled PLA, SiO_2, $CaCO_3$, and $BaCO_3$ NPs. As shown in Fig. 5b, the cellular uptake efficiency (C_{NPs}=8 mg/mL) was 86.31% for $CaCO_3$, 85.97% for $BaCO_3$, 69.95% for PLA, and 59.89% for SiO_2. Figure S18a (supplementary information) shows the cellular uptake efficiency for C_{NPs}=4 mg/mL.

The internalization and penetration efficiency of the Cy5_NPs were then estimated in a 3D cell culture using a tumor spheroid model. Figure S17 (supplementary information) displays the tumor spheroid preparation scheme. The tumor spheroid model mimics the extracellular environment of solid tumors [52−54]. Figure S18b (supplementary information) shows merged CLSM images of tumor spheroids incubated with the Cy5_NPs at a 10–100 μm penetration depth for 24 h. Unmerged CLSM images and quantitative analysis of the penetration depth of the NPs within tumor spheroids are presented in Figs. 5c–5e. The Cy5_NPs demonstrated high penetration efficiency into the tumor; i.e., SiO_2, $CaCO_3$, and $BaCO_3$ NPs penetrated to depths >80 μm, while the PLA NPs penetrated to approximately 70 μm.

The in vitro antitumor efficiency of 2AmT-loaded NPs was investigated using the Alamar Blue assay. Figure 5f shows viability histograms of B16-F10 cells as a function of the 2AmT amount. The 2AmT-loaded NPs exhibited a dose-dependent cytotoxicity. In particular, the viability of B16-F10 cells incubated with 2AmT_NPs at 7.5 μmol/L was <50% and continued to decrease at high 2AmT_NP concentrations (30 μmol/L). The cellular localization of the 2AmT compound was verified by CLSM imaging (Fig. S19 in the supplementary information). The NPs and PEI-coated NPs without drug loading demonstrated nontoxic effects on B16-F10 cells (Fig. S20 in the supplementary information). Additionally, changes in cell morphology and adherent state were observed using optical microscopy (Figs. S21−S24 in the supplementary information). The optical images showed unhealthy cellular morphology, characterized by shrunken and detached cells, following treatment with 2AmT_NPs.

The impact of the developed NPs and 2AmT_NPs on RBC destruction was also investigated using a hemolysis assay (Fig. S25 in the supplementary information). These NPs exhibited no significant toxicity toward RBCs.

3.5 In vivo biodistribution analysis

The scheme of the in vivo NP biodistribution analysis is illustrated in Fig. 6a. Cy5-labeled NPs were used for fluorescent bioimaging, and ^{99m}Tc-labeled NPs (^{99m}Tc_NPs) were applied for SPECT imaging. The radiolabeling procedure is described in Sect. S10 (supplementary information). The high radiolabeling efficiency and retention of the ^{99m}Tc isotope were confirmed (Fig. S26 in the supplementary information). Figure 6b1 displays fluorescent images of tumor-bearing mice 48 h after injection of the Cy5_NPs. Fluorescence from the Cy5_NPs over 4−8 d is presented in Fig. S27 (supplementary information). Fluorescent signals within the tumor site for all tested NPs were clearly detected. Detailed analysis of tumors extracted on 8 d post-injection showed different localizations of the Cy5_NPs (Fig. 6b2). In particular, the Cy5_$CaCO_3$ NPs almost entirely covered the tumor volume, whereas the Cy5_PLA, Cy5_SiO_2, and Cy5_$BaCO_3$ NPs were only partly distributed within the tumors. The quantitative data (fluorescent intensity) showed that Cy5_$CaCO_3$ NPs exhibited the greatest increase compared to the other NPs ((88±9) arbitrary units (a.u.) for Cy5_PLA, (157±16) a.u. for Cy5_SiO_2, (884±88) a.u. for Cy5_$CaCO_3$, and (388±39) a.u. for Cy5_$BaCO_3$ NPs). Furthermore, SPECT imaging of mice injected with ^{99m}Tc_NPs is shown in Fig. 6c1. The unchanged position of radiolabeled NPs was observed in the tumor for all tested NPs over 48 h. The direct radiometry data fully supported the results of the SPECT imaging (Fig. 6c2). All ^{99m}Tc_NPs expressed the most significant signals at the tumor site (ID/g approximately 99%) and signals of <1% for the main organs (heart, lungs, liver, spleen, and kidneys). Finally, fluorescence analysis of tumor tissues showed the presence of Cy5_NPs agglomerates (Fig. 6d).

3.6 Localized chemotherapy analysis

The therapeutic efficiency of the 2AmT-loaded PLA, SiO_2, $CaCO_3$, and $BaCO_3$ NPs was compared in the B16-F10 melanoma model. When the tumors reached approximately (0.05±0.01) cm^3, the NPs were intratumorally injected with 2AmT at 0.2 g/kg and 0.4 g/kg. In general, intravenous injections are used for NP delivery in tumor therapy. However, this type of injection often limits uptake within target tumors due to sequestration by the reticuloendothelial system in organs. This limitation can be addressed by local NP injection. The main benefits of intratumoral NP injection include enhanced therapeutic effect and reduced patient

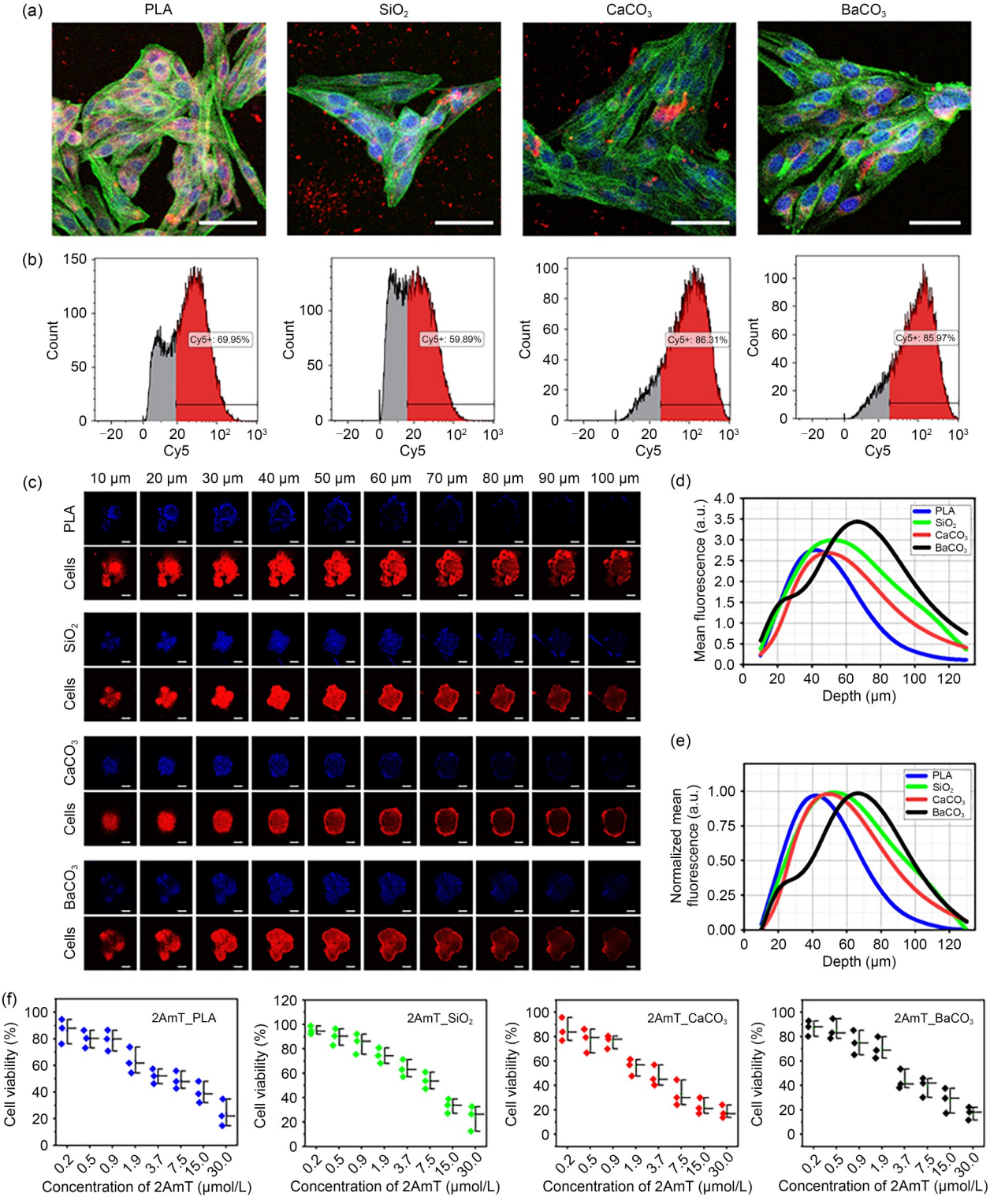

Fig. 5 In vitro performance of PLA, SiO_2, $CaCO_3$, and $BaCO_3$ NPs. (a) CLSM images of B16-F10 cells incubated with the Cy5-labeled PLA, SiO_2, $CaCO_3$, and $BaCO_3$ NPs (8 mg/mL). Cell cytoskeletons were stained with phalloidin-FITC (green), the nuclei were marked with PI (blue), and Cy5_NPs were marked as red signals. Scale bars: 50 μm. (b) Flow cytometry analysis of the cellular association of the Cy5-labeled PLA, SiO_2, $CaCO_3$, and $BaCO_3$ NPs (8 mg/mL) in B16-F10 cells after 24 h of incubation. (c) CLSM images of the fluorescence distribution of Cy5-labeled NPs within tumor spheroids for 24 h. Scale bars: 150 μm. NPs were labeled with Cy5 (blue), and the cells inside the tumor spheroids were stained with PI (red). (d) Cy5_NPs fluorescence signals as a function of penetration depth within the spheroid. (e) Graphs of normalized mean fluorescence at different depths within the spheroid. (f) Viability histograms of B16-F10 cells treated with the 2AmT-loaded PLA, SiO_2, $CaCO_3$, and $BaCO_3$ NPs. The results are shown as mean±standard deviation (n=3)

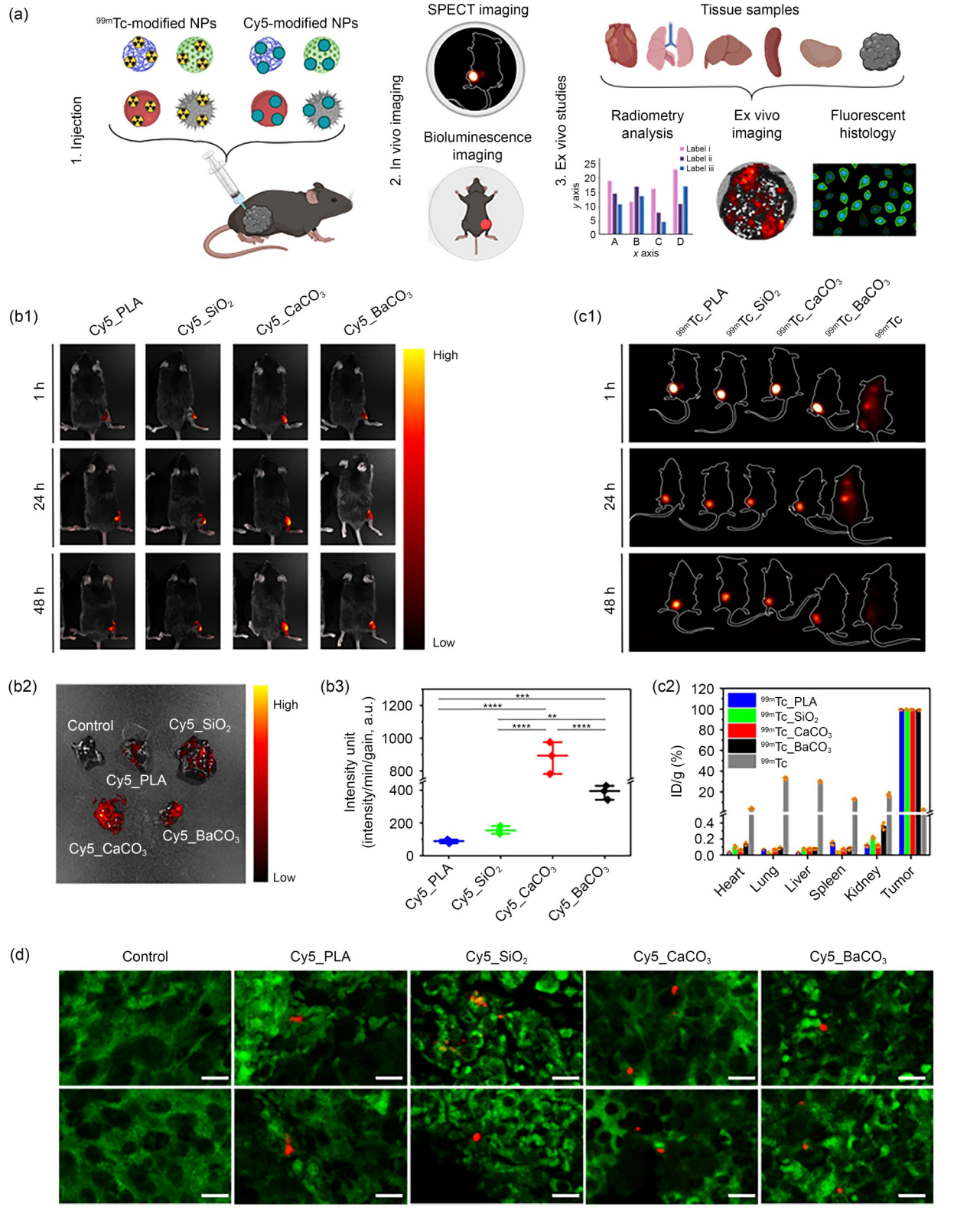

Fig. 6 In vivo biodistribution efficiency of the PLA, SiO_2, $CaCO_3$, and $BaCO_3$ NPs. (a) The in vivo experiments included NP injection, fluorescent bioimaging, SPECT imaging, and fluorescent histological analysis. (b1) Fluorescent bioimaging of mice after Cy5_NP injection. (b2, b3) Ex vivo fluorescence bioimaging analysis of extracted tumors with corresponding quantitative assessment for Cy5_NPs 8 d after injection. (c1) SPECT images of tumor-bearing mice after ^{99m}Tc_NP injection. (c2) Direct radiometry analysis of ex vivo organs (heart, lungs, liver, spleen, and kidneys) and tumors. (d) Fluorescent histological analysis of tumor tissues (green) after injection of Cy5_NPs (red). Scale bars: 10 μm. The results are shown as mean±standard error of the mean (n=3). $^{**}p<0.01$, $^{***}p<0.001$, and $^{****}p<0.0001$

morbidity [55, 56]. Furthermore, NP use for intratumoral injection offers the following advantages: (1) a high local concentration of the drug in the tumor; (2) prolonged drug release; and (3) reduced side effects [57]. For these reasons, intratumoral NP injection was selected. All tested groups and the therapeutic scheme are illustrated in Fig. 7a. The following experimental groups were tested: Control (PBS), 2AmT (0.2 g/kg and 0.4 g/kg); 2AmT_PLA (0.2 g/kg and 0.4 g/kg); 2AmT_SiO_2 (0.2 g/kg and 0.4 g/kg); 2AmT_$CaCO_3$ (0.2 g/kg and 0.4 g/kg); and 2AmT_$BaCO_3$ (0.2 g/kg and 0.4 g/kg). Figure 7b and Fig. S29a (supplementary information) display changes in tumor size during the treatment period. Digital photos of the mice are shown in Fig. S28 (supplementary information). The 2AmT_NPs significantly reduced the tumor volumes. In contrast, tumors rapidly grew in control (nontreated) mice and in the 2AmT (0.2 g/kg) group. Importantly, no significant loss of body weight was detected for any of the tested groups (Fig. 7c; Fig. S29b in the supplementary information). At the end of the treatment, the mice were sacrificed and the tumors were extracted for further investigation (Fig. 7d; Fig. S29c in the supplementary information). The sizes of the extracted tumors were measured (Fig. 7e; Fig. S29d in the supplementary information). The control combines the results for all nontreated mice. Therefore, the control group contains 8 experimental dots. Based on these results, the therapeutic efficiency of 2AmT_NPs on tumor growth inhibition was: $CaCO_3$ (87.9%–93.4% for 0.4 g/kg 2AmT)>SiO_2 (75.6%–93.2% for 0.4 g/kg 2AmT)>PLA (80.3%–88.2% for 0.4 g/kg 2AmT)>$BaCO_3$ (58.8%–83.7% for 0.4 g/kg 2AmT). Although the differences are not statistically significant due to overlapping error bars, the measured values differ. Furthermore, the in vivo therapeutic effect was investigated with H&E staining. H&E-stained tumor images for all tested groups are presented in Fig. 7f and Fig. S30 (supplementary information). The H&E staining results for the control (PBS) group demonstrated aggressive invasive tumor growth, significant infiltration of surrounding tissues, spontaneous mitosis, and extensive melanin deposits. In contrast, the 2AmT-treated groups were characterized by a significant decrease in tumor mass, with a noticeable reduction in active proliferation and invasion of tumor cells into healthy tissues.

Furthermore, H&E staining of the main organs (heart, lungs, liver, spleen, and kidneys) was performed to assess any toxicity of the developed NPs following therapy. Figure 8 shows the images of the H&E staining of organs from animals that were exposed to all the NPs. Fluorescence microscopic images of the tissues in the organs were also obtained. Additional representative images of the H&E staining of the organs are provided in Fig. S31 (supplementary information). From the results obtained, there were no observable histopathological changes in the examined tissues in the organs. It is worth mentioning that the cardiovascular system exhibited normal architecture without myocardium and endocardium pathology. Moreover, vascular structures were intact, and alveoli and pleural tissues were not affected. In addition, the liver architecture was normal with normal hepatocytes. The spleen exhibited moderate blood flow in the red pulp and normal architecture in the white pulp. Renal tissues were also normal without any pathological features.

3.7 Analysis of the NPs with unique physicochemical features and their therapeutic effectiveness

Table 3 summarizes the characteristics tested for the developed NPs. We considered and compared the following parameters: visual evaluation, NP morphology, size of the developed NPs, surface properties (BET and pore size), colloidal stability, cumulative drug release, tumor penetration, tumor localization, and tumor response.

According to the results in Table 3, the following observations can be made. All NP suspensions looked similar, as stable turbid suspensions without aggregates. The average NP size was around 100 nm, and only the SiO_2 NPs were smaller than 100 nm. However, the average D_h values of the developed NPs were very similar, in the range of 235–255 nm. Therefore, the similar D_h of NPs with different chemical compositions allows us to compare them. When analyzing surface properties, the BET surface areas of SiO_2 and $BaCO_3$ NPs were notably higher than that of the $CaCO_3$ NPs, which exhibited a lower surface area of 51.05 m^2/g. Meanwhile, the pore size was almost the same for all NPs. The drug-loading capacity does not depend on the NP surface area or pore size. Despite the difference in surface properties, the drug loading of 2AmT was similar for all NP types: (66.71±1.99)% (PLA NPs), (74.15±3.74)% (SiO_2 NPs), (75.29±3.56)% ($CaCO_3$ NPs), and (72.71±4.44)% ($BaCO_3$ NPs).

Regarding NP colloidal stability, at the initial time, the average D_h values were similar across all NPs. However, the colloidal stability (ΔD_h) of these NPs is entirely different and depends on their chemical composition. The PLA and SiO_2 NPs tended to exhibit high colloidal stability. Meanwhile, the $CaCO_3$ and $BaCO_3$ NPs remained less stable, especially in acidic solutions. This may be associated with the partial dissolution of $CaCO_3$ and $BaCO_3$ NPs in acidic conditions, which leads to their destabilization and partial aggregation [58–60]. These findings are critical for translating laboratory protocols on NP synthesis into large-scale manufacturing. We suggest using additional organic additives to stabilize $CaCO_3$ and $BaCO_3$ NPs for long-term storage, although this may complicate synthesis processing methods.

Cumulative drug release depends on the pH. The highest release efficiency was observed for the $CaCO_3$ and $BaCO_3$

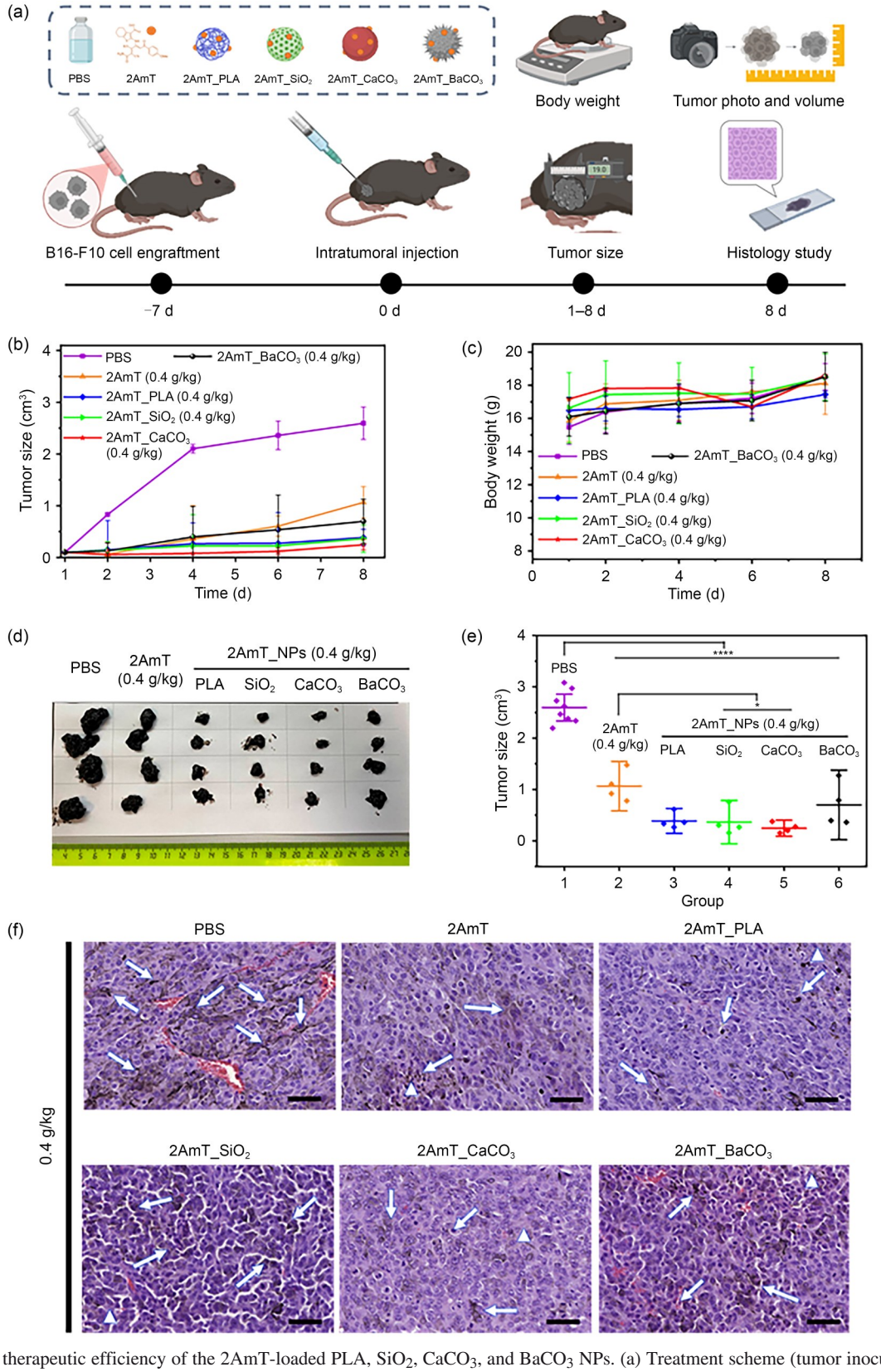

Fig. 7 In vivo therapeutic efficiency of the 2AmT-loaded PLA, SiO_2, $CaCO_3$, and $BaCO_3$ NPs. (a) Treatment scheme (tumor inoculation, injection of NPs (0.4 g/kg 2AmT), body weight and tumor size measurement, and histological analysis). (b) Tumor size measurement during therapy. (c) The body weight of the mice was measured during therapy. (d) Digital photos of tumors extracted from the sacrificed mice. (e) Tumor size determined on 8 d of therapy. (f) Images of H&E-stained tumors after therapy (→ extensive melanin deposits; ▲ tumor necrosis). Scale bars: 50 μm. The results are shown as mean±standard error of the mean (n=4). $^{*}p<0.05$ and $^{****}p<0.0001$

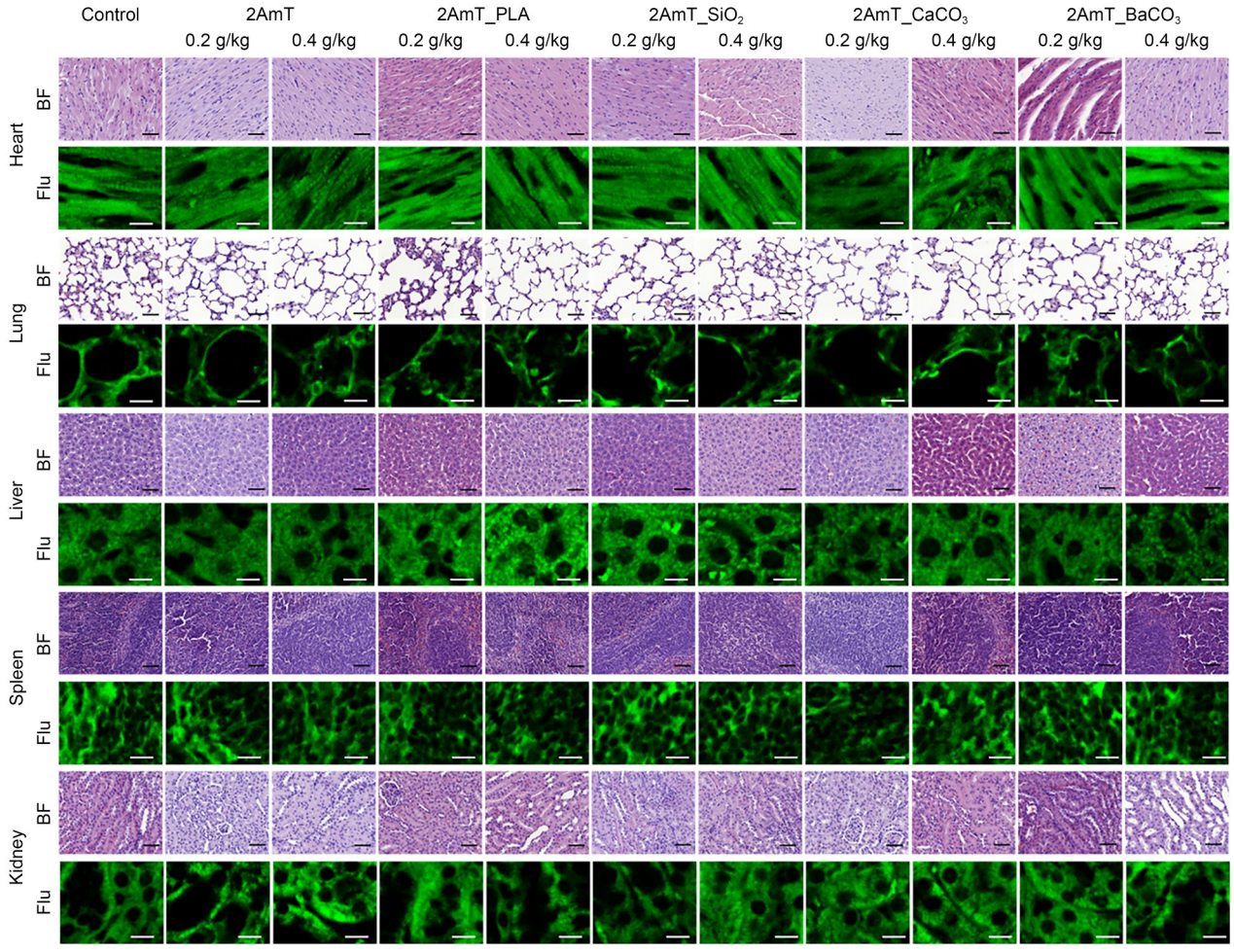

Fig. 8 Bright-field (BF) and fluorescent (Flu) images of H&E-stained tissues from the primary organs (heart, lungs, liver, spleen, and kidneys) of mice after treatment with each tested group (control, 2AmT (0.2 and 0.4 g/kg), 2AmT_PLA (0.2 and 0.4 g/kg), 2AmT_SiO_2 (0.2 and 0.4 g/kg), 2AmT_$CaCO_3$ (0.2 and 0.4 g/kg), and 2AmT_$BaCO_3$ (0.2 and 0.4 g/kg)). Scale bars: 50 μm for BF and 10 μm for Flu

NPs under acidic conditions (approximately 39%–40%, determined for a 0.1% BSA solution, pH 3.5). This tendency can be explained by the partial dissolution of $CaCO_3$ and $BaCO_3$ NPs in acidic conditions [58–60]. The high drug release capacity of the $CaCO_3$ and $BaCO_3$ NPs is a beneficial characteristic for DDSs, enabling the delivery of the maximum therapeutic dose. The pH-responsive NPs have drawn significant attention as stimulus-sensitive DDSs. Furthermore, the partial dissolution of the $CaCO_3$ and $BaCO_3$ NPs may influence their fast degradation and removal from the organism.

The tumor penetration efficiency (in vitro) was very similar for the SiO_2, $CaCO_3$, and $BaCO_3$ NPs. However, the PLA NPs exhibited the lowest tumor penetration. In tumor-localization studies (in vivo), the most significant results were observed for the $CaCO_3$ NPs, whereas less tumor localization was detected for the PLA, SiO_2, and $BaCO_3$ NPs. Thus, the efficiency of NP tumor localization was in the following order: $CaCO_3$>$BaCO_3$>SiO_2>PLA. This parameter may directly contribute to enhanced tumor therapy. Indeed, the high tumor localization of NPs enables sustained diffusion and penetration of the released drug into a tumor.

Comparing the results for colloidal stability, drug release, tumor penetration, and localization, the $CaCO_3$ NPs have the most appropriate characteristics for melanoma therapy. 2AmT-loaded $CaCO_3$ NPs displayed the narrowest therapeutic range for melanoma at 0.4 g/kg of loaded 2AmT (87.9%–93.4%), suggesting good reproducibility of therapeutic efficiency. In summary, there is a clear correlation between the main NP parameters (colloidal stability, cumulative release, tumor penetration, and tumor localization) and therapeutic effectiveness. These parameters are critical for the future design and manufacturing of novel nanocarriers.

4 Conclusions

This study provided a comprehensive comparison of the designed NPs with unique physicochemical features and their

Table 3 Comparison of physicochemical parameters (size, morphology, colloidal stability, drug-loading and release efficiency), in vitro performance, and in vivo therapeutic efficiency of the PLA, SiO_2, $CaCO_3$, and $BaCO_3$ NPs

Parameter	PLA NPs	SiO_2 NPs	$CaCO_3$ NPs	$BaCO_3$ NPs
Visual evaluation	Slightly turbid white suspension	Turbid white suspension	Turbid white suspension	Turbid white suspension
NPs morphology	Nanospheres with slight polydispersity	Monodisperse solid nanospheres	Homogeneous nanospheres with minimal surface irregularities	Homogeneous nanospheres with a compact structure and bulges on the surface
NPs size (nm)	The obtained average size using SEM			
	~130	~90	~120	~140
	Determined D_h for 0.9% NaCl solution (pH 7.0)			
	~244	~255	~235	~254
BET (m^2/g)	–	98.93	51.05	84.38
Pore size (nm)	–	3.2	3.5	<2
[a] In vitro colloidal stability for 18 d (nm)	ΔD_h calculated for 0.9% NaCl solution (pH 3.5)			
	~166	~156	~242	~208
	ΔD_h calculated for 0.9% NaCl solution (pH 7.0)			
	~144	~136	~104	~179
	ΔD_h calculated for 0.1% BSA solution (pH 3.5)			
	~166	~127	~182	~263
	ΔD_h calculated for 0.1% BSA solution (pH 7.0)			
	~182	~126	~182	~227
Cumulative release efficiency (%)	Determined for 0.9% NaCl solution (pH 3.5)			
	17.79±1.60	19.92±2.00	27.58±1.93	17.29±1.73
	Determined for 0.9% NaCl solution (pH 7.0)			
	3.11±0.78	3.64±0.91	7.65±1.53	12.68±1.27
	Determined for 0.1% BSA solution (pH 3.5)			
	11.36±1.02	8.08±0.97	40.11±2.01	39.98±2.40
	Determined for 0.1% BSA solution (pH 7.0)			
	3.42±0.85	5.32±1.33	6.56±1.31	18.88±1.89
[b] Tumor penetration efficiency (μm)	~70	~95	~85	~98
[c] Relative tumor localization (a.u.)	~88	~157	~884	~388
[d] Tumor response (%)	Determined for 0.2 g/kg of 2AmT			
	56.6–71.7	70.2–79.5	76.7–83.2	65.4–78.7
	Determined for 0.4 g/kg of 2AmT			
	80.3–88.2	75.6–93.2	87.9–93.4	58.8–83.7

[a] $\Delta D_h = D_{h\,max} - D_{h\,min}$; [b] Tumor penetration efficiency was determined as the half-height of the normalized mean fluorescence of the unmerged images (Fig. 5e); [c] Relative tumor localization was calculated as intensity unit (intensity/min/gain) of Cy5_NPs; [d] Tumor response was determined using the following equations: $(1-max_{sample}/max_{control})\times100\%$ and $(1-min_{sample}/min_{control})\times100\%$, where max_{sample} and min_{sample} are the maximum and minimum tumor sizes within a specific treatment group, while $max_{control}$ and $min_{control}$ are the corresponding values in the control group

therapeutic effectiveness against melanoma. Overall, the main criteria responsible for therapeutic effectiveness include colloidal stability, drug-loading and release efficiency, tumor penetration, and tumor localization. Colloidal stability is a key characteristic in NP design that affects NP storage and delivery efficiency. Based on our investigation, PLA and SiO_2 NPs demonstrated the highest colloidal stability for long-term storage. However, the cumulative release efficiency of 2AmT was higher for the $CaCO_3$ and $BaCO_3$ NPs. The tumor localization efficiency was the highest for the $CaCO_3$ NPs. These criteria play a significant role in the therapeutic effect, and insufficient consideration of these factors

limits the applicability of designed NPs in clinical practice. We found that $CaCO_3$ NPs exhibited the most appropriate therapeutic effect (87.9%–93.4% for 0.4 g/kg of 2AmT) compared to PLA (80.3%–88.2% for 0.4 g/kg of 2AmT), SiO_2 (75.6%–93.2% for 0.4 g/kg of 2AmT), and $BaCO_3$ (58.8%–83.7% for 0.4 g/kg of 2AmT). These results contribute to the scientific community by highlighting the role of nanocarrier design and manufacturing in achieving maximum therapeutic efficiency against melanoma and may accelerate the translation of NPs into clinical practice.

Supplementary Information The online version contains supplementary material available at https://doi.org/10.1631/bdm.2500283.

Acknowledgements The work related to the synthesis of NPs was supported by the Russian Science Foundation (No. 25-15-20047) and the St. Petersburg Science Foundation. The research related to in vitro and in vivo studies was conducted with the financial support of the Ministry of Science and Higher Education of the Russian Federation (No. FSEG-2025-0007). We thank the research center of ITMO University for SEM imaging and BET analysis. The authors would like to thank the Granov Russian Research Center for its support in the radiological experiments and Peter the Great St. Petersburg Polytechnic University for providing the research facilities used for particle synthesis, in vitro, in vivo studies, and animal ethics approval. The graphical elements from Figs. 1, 4, 6, 7, and Figs. S17 and S26 (supplementary information) were created with BioRender.com.

Author contributions TEK: investigation, data interpretation, writing—original draft, and final approval of the version to be published. YAT and SVF: synthesis of NPs and their characterization. IAG: synthesis and characterization of 2AmT. AR: in vitro experiment, in vivo experiment, and histology studies. TSC: surface characterization of NPs. KC: PXRD analysis of NPs. RRS: cell toxicity of NPs after PEI coating. ASK, EJP, ING, and AIS: FACS analysis. SAS and AST: editing and writing the manuscript, final approval of the version to be published, and supervision. All authors agree to be accountable for all aspects of the work.

Declarations

Conflict of interest The authors declare that they have no conflict of interest.

Ethical approval All animal procedures were performed in accordance with the Guidelines for Care and Use of Laboratory Animals of Peter the Great St. Petersburg Polytechnic University and approved by the local Animal Ethics Committee of the Institute of Biomedical Systems and Biotechnology of Peter the Great St. Petersburg Polytechnic University. The composition of the local Animal Ethics Committee was approved by Order No. 21 dated 26 February 2020. The ethical approval order was No. 01, dated 3 February 2025.

Data availability Data will be made available on request.

Use of generative AI tools No generative AI tools were used in the preparation of this manuscript.

References

1. Liz-Marzán LM, Nel AE, Brinker CJ et al (2022) What do we mean when we say nanomedicine? *ACS Nano* 16(9):13257–13259. https://doi.org/10.1021/acsnano.2c08675
2. Gavas S, Quazi S, Karpiński TM (2021) Nanoparticles for cancer therapy: current progress and challenges. *Nanoscale Res Lett* 16(1):173. https://doi.org/10.1186/s11671-021-03628-6
3. Sun LM, Liu HM, Ye YQ et al (2023) Smart nanoparticles for cancer therapy. *Signal Transduct Target Ther* 8(1):418. https://doi.org/10.1038/s41392-023-01642-x
4. Liu R, Luo C, Pang ZQ et al (2023) Advances of nanoparticles as drug delivery systems for disease diagnosis and treatment. *Chin Chem Lett* 34(2):107518. https://doi.org/10.1016/j.cclet.2022.05.032
5. Hua Y, Qin ZB, Gao L et al (2024) Protein nanoparticles as drug delivery systems for cancer theranostics. *J Control Release* 371:429–444. https://doi.org/10.1016/j.jconrel.2024.06.004
6. Geszke-Moritz M, Moritz M (2024) Biodegradable polymeric nanoparticle-based drug delivery systems: comprehensive overview, perspectives and challenges. *Polymers* 16(17):2536. https://doi.org/10.3390/polym16172536
7. Chen SL, Luo Y, He Y et al (2024) In-situ-sprayed therapeutic hydrogel for oxygen-actuated Janus regulation of postsurgical tumor recurrence/metastasis and wound healing. *Nat Commun* 15(1):814. https://doi.org/10.1038/s41467-024-45072-x
8. Beola L, Iturrioz-Rodríguez N, Pucci C et al (2023) Drug-loaded lipid magnetic nanoparticles for combined local hyperthermia and chemotherapy against glioblastoma multiforme. *ACS Nano* 17(18):18441–18455. https://doi.org/10.1021/acsnano.3c06085
9. Li ZM, Yang Y, Wei HX et al (2021) Charge-reversal biodegradable MSNs for tumor synergetic chemo/photothermal and visualized therapy. *J Control Release* 338:719–730. https://doi.org/10.1016/j.jconrel.2021.09.005
10. Zeb A, Gul M, Nguyen TTL et al (2022) Controlled release and targeted drug delivery with poly(lactic-co-glycolic acid) nanoparticles: reviewing two decades of research. *J Pharm Investig* 52(6):683–724. https://doi.org/10.1007/s40005-022-00584-w
11. De R, Mahata MK, Kim KT (2022) Structure-based varieties of polymeric nanocarriers and influences of their physicochemical properties on drug delivery profiles. *Adv Sci* 9(10):2105373. https://doi.org/10.1002/advs.202105373
12. Tian YC, Cheng TF, Sun FW et al (2024) Effect of biophysical properties of tumor extracellular matrix on intratumoral fate of nanoparticles: implications on the design of nanomedicine. *Adv Colloid Interface Sci* 326:103124. https://doi.org/10.1016/j.cis.2024.103124
13. He HL, Liu LS, Morin EE et al (2019) Survey of clinical translation of cancer nanomedicines: lessons learned from successes and failures. *Acc Chem Res* 52(9):2445–2461. https://doi.org/10.1021/acs.accounts.9b00228
14. Mendes BB, Zhang ZL, Conniot J et al (2024) A large-scale machine learning analysis of inorganic nanoparticles in preclinical cancer research. *Nat Nanotechnol* 19(6):867–878. https://doi.org/10.1038/s41565-024-01673-7
15. Sindhwani S, Syed AM, Ngai J et al (2020) The entry of nanoparticles into solid tumours. *Nat Mater* 19(5):566–575. https://doi.org/10.1038/s41563-019-0566-2
16. Nguyen LNM, Lin ZP, Sindhwani S et al (2023) The exit of nanoparticles from solid tumours. *Nat Mater* 22(10):1261–1272. https://doi.org/10.1038/s41563-023-01630-0
17. Cheng YH, He CL, Riviere JE et al (2020) Meta-analysis of nanoparticle delivery to tumors using a physiologically based pharmacokinetic modeling and simulation approach. *ACS Nano* 14(3):3075–3095.

https://doi.org/10.1021/acsnano.9b08142
18. Nguyen LNM, Ngo W, Lin ZP et al (2024) The mechanisms of nanoparticle delivery to solid tumours. *Nat Rev Bioeng* 2(3): 201–213. https://doi.org/10.1038/s44222-024-00154-9
19. Perry JL, Reuter KG, Luft JC et al (2017) Mediating passive tumor accumulation through particle size, tumor type, and location. *Nano Lett* 17(5):2879–2886. https://doi.org/10.1021/acs.nanolett.7b00021
20. Lee D, Huntoon K, Lux J et al (2023) Engineering nanomaterial physical characteristics for cancer immunotherapy. *Nat Rev Bioeng* 1(7):499–517. https://doi.org/10.1038/s44222-023-00047-3
21. Agnihotri TG, Alexander A, Agrawal M et al (2023) *In vitro-in vivo* correlation in nanocarriers: from protein corona to therapeutic implications. *J Control Release* 354:794–809. https://doi.org/10.1016/j.jconrel.2023.01.063
22. Vallet-Regí M, Schüth F, Lozano D et al (2022) Engineering mesoporous silica nanoparticles for drug delivery: where are we after two decades? *Chem Soc Rev* 51(13):5365–5451. https://doi.org/10.1039/d1cs00659b
23. Yang XR, Sun Y, Zhang H et al (2024) $CaCO_3$ nanoplatform for cancer treatment: drug delivery and combination therapy. *Nanoscale* 16(14):6876–6899. http://doi.org/10.1039/d3nr05986c
24. Sahini MG (2023) Polylactic acid (PLA)-based materials: a review on the synthesis and drug delivery applications. *Emergent Mater* 6(5):1461–1479. https://doi.org/10.1007/s42247-023-00551-7
25. Wang Y, Qin B, Xia G et al (2021) FDA's poly (lactic-co-glycolic acid) research program and regulatory outcomes. *AAPS J* 23(4):92. https://doi.org/10.1208/s12248-021-00611-y
26. Dillman JR, Towbin AJ, Imbus R et al (2018) Comparison of two neutral oral contrast agents in pediatric patients: a prospective randomized study. *Radiology* 288(1):245–251. https://doi.org/10.1148/radiol.2018173039
27. D'Aguanno S, Mallone F, Marenco M et al (2021) Hypoxia-dependent drivers of melanoma progression. *J Exp Clin Cancer Res* 40(1):159. https://doi.org/10.1186/s13046-021-01926-6
28. Fang YL, Huang SS, Hu QY et al (2023) Injectable zwitterionic physical hydrogel with enhanced chemodynamic therapy and tumor microenvironment remodeling properties for synergistic anticancer therapy. *ACS Nano* 17(24):24883–24900. https://doi.org/10.1021/acsnano.3c05898
29. Rogova A, Gorbunova IA, Karpov TE et al (2023) Synthesis of thieno[3,2-*e*]pyrrolo[1,2-*a*]pyrimidine derivatives and their precursors containing 2-aminothiophenes fragments as anticancer agents for therapy of pulmonary metastatic melanoma. *Eur J Med Chem* 254:115325. https://doi.org/10.1016/j.ejmech.2023.115325
30. Chorny M, Fishbein I, Danenberg HD et al (2002) Lipophilic drug loaded nanospheres prepared by nanoprecipitation: effect of formulation variables on size, drug recovery and release kinetics. *J Control Release* 83(3):389–400. https://doi.org/10.1016/S0168-3659(02)00211-0
31. Bahrom H, Goncharenko AA, Fatkhutdinova LI et al (2019) Controllable synthesis of calcium carbonate with different geometry: comprehensive analysis of particle formation, cellular uptake, and biocompatibility. *ACS Sustainable Chem Eng* 7(23):19142–19156. https://doi.org/10.1021/acssuschemeng.9b05128
32. Xu CY, Yan YF, Tan JC et al (2019) Biodegradable nanoparticles of polyacrylic acid–stabilized amorphous $CaCO_3$ for tunable pH-responsive drug delivery and enhanced tumor inhibition. *Adv Funct Mater* 29(24):1808146. https://doi.org/10.1002/adfm.201808146
33. Fennema E, Rivron N, Rouwkema J et al (2013) Spheroid culture as a tool for creating 3D complex tissues. *Trends Biotechnol* 31(2):108–115. https://doi.org/10.1016/j.tibtech.2012.12.003
34. Dobrovolskaia MA, Clogston JD, Neun BW et al (2008) Method for analysis of nanoparticle hemolytic properties in vitro. *Nano Lett* 8(8):2180–2187. https://doi.org/10.1021/nl0805615
35. Zhuravlev YN, Atuchin VV (2020) Comprehensive density functional theory studies of vibrational spectra of carbonates. *Nanomaterials* 10(11):2275. https://doi.org/10.3390/nano10112275
36. Li JZ, Guo X, Panchal B et al (2024) Quantitative analysis of molecular structure characterization of different liptinite-rich coals using FTIR spectroscopy. *Infrared Phys Technol* 141:105458. https://doi.org/10.1016/j.infrared.2024.105458
37. Al-Bermany E, Mekhalif AT, Banimuslem HA et al (2023) Effect of green synthesis bimetallic $Ag@SiO_2$ core–shell nanoparticles on absorption behavior and electrical properties of PVA-PEO nanocomposites for optoelectronic applications. *Silicon* 15(9): 4095–4107. https://doi.org/10.1007/s12633-023-02332-7
38. Ruiz E, Orozco VH, Hoyos LM et al (2022) Study of sonication parameters on PLA nanoparticles preparation by simple emulsion-evaporation solvent technique. *Eur Polym J* 173:111307. https://doi.org/10.1016/j.eurpolymj.2022.111307
39. Li CC, Jean JH (2002) Dissolution and dispersion behavior of barium carbonate in aqueous suspensions. *J Am Ceram Soc* 85(12): 2977–2983. https://doi.org/10.1111/j.1151-2916.2002.tb00566.x
40. Ouyang J, Mu DW, Zhang Y et al (2018) Selective fabrication of barium carbonate nanoparticles in the lumen of halloysite nanotubes. *Minerals* 8(7):296. https://doi.org/10.3390/min8070296
41. Lauth V, Maas M, Rezwan K (2017) An evaluation of colloidal and crystalline properties of $CaCO_3$ nanoparticles for biological applications. *Mater Sci Eng C* 78:305–314. https://doi.org/10.1016/j.msec.2017.04.037
42. Moulin P, Roques H (2003) Zeta potential measurement of calcium carbonate. *J Colloid Interface Sci* 261(1):115–126. https://doi.org/10.1016/S0021-9797(03)00057-2
43. Parizad A, Shahbazi K, Tanha AA (2018) SiO_2 nanoparticle and KCl salt effects on filtration and thixotropical behavior of polymeric water based drilling fluid: with zeta potential and size analysis. *Results Phys* 9:1656–1665. https://doi.org/10.1016/j.rinp.2018.04.037
44. Sarasua JR, Prud'homme RE, Wisniewski M et al (1998) Crystallization and melting behavior of polylactides. *Macromolecules* 31(12):3895–3905. https://doi.org/10.1021/ma971545p
45. Hu Y, Cao C, Zhang L et al (2024) Synthesis of silica particles with controlled microstructure via the choline hydroxide cocatalyzed Stöber method. *Langmuir* 40(30):15933–15940. https://doi.org/10.1021/acs.langmuir.4c02025
46. Wang J, Wang D, Cen MP et al (2022) GOx-assisted synthesis of pillar[5]arene based supramolecular polymeric nanoparticles for targeted/synergistic chemo-chemodynamic cancer therapy. *J Nanobiotechnol* 20(1):33. https://doi.org/10.1186/s12951-021-01237-0
47. Shen HJ, Shi H, Ma K et al (2013) Polyelectrolyte capsules packaging BSA gels for pH-controlled drug loading and release and their antitumor activity. *Acta Biomater* 9(4):6123–6133. https://doi.org/10.1016/j.actbio.2012.12.024

48. Fu JL, Leo CP, Show PL (2022) Recent advances in the synthesis and applications of pH-responsive $CaCO_3$. *Biochem Eng J* 187:108446. https://doi.org/10.1016/j.bej.2022.108446
49. Niu YQ, Liu JH, Aymonier C et al (2022) Calcium carbonate: controlled synthesis, surface functionalization, and nanostructured materials. *Chem Soc Rev* 51(18):7883–7943. https://doi.org/10.1039/d1cs00519g
50. Kaspchak E, Goedert AC, Igarashi-Mafra L et al (2019) Effect of divalent cations on bovine serum albumin (BSA) and tannic acid interaction and its influence on turbidity and *in vitro* protein digestibility. *Int J Biol Macromol* 136:486–492. https://doi.org/10.1016/j.ijbiomac.2019.06.102
51. Bilardo R, Traldi F, Vdovchenko A et al (2022) Influence of surface chemistry and morphology of nanoparticles on protein corona formation. *Wires Nanomed Nanobiotechnol* 14(4):e1788. https://doi.org/10.1002/wnan.1788
52. Li WX, Zhou ZH, Zhou XY et al (2023) 3D biomimetic models to reconstitute tumor microenvironment in vitro: spheroids, organoids, and tumor-on-a-chip. *Adv Healthc Mater* 12(18):2202609. https://doi.org/10.1002/adhm.202202609
53. Mangani S, Kremmydas S, Karamanos NK (2025) Mimicking the complexity of solid tumors: how spheroids could advance cancer preclinical transformative approaches. *Cancers* 17(7):1161. https://doi.org/10.3390/cancers17071161
54. Rodrigues DB, Reis RL, Pirraco RP (2024) Modelling the complex nature of the tumor microenvironment: 3D tumor spheroids as an evolving tool. *J Biomed Sci* 31(1):13. https://doi.org/10.1186/s12929-024-00997-9
55. Wolinsky JB, Colson YL, Grinstaff MW (2012) Local drug delivery strategies for cancer treatment: gels, nanoparticles, polymeric films, rods, and wafers. *J Control Release* 159(1):14–26. https://doi.org/10.1016/j.jconrel.2011.11.031
56. Llovet JM, De Baere T, Kulik L et al (2021) Locoregional therapies in the era of molecular and immune treatments for hepatocellular carcinoma. *Nat Rev Gastroenterol Hepatol* 18(5):293–313. https://doi.org/10.1038/s41575-020-00395-0
57. Bhardwaj P, Gota V, Vishwakarma K et al (2022) Loco-regional radiosensitizing nanoparticles-in-gel augments head and neck cancer chemoradiotherapy. *J Control Release* 343:288–302. https://doi.org/10.1016/j.jconrel.2022.01.040
58. Maleki Dizaj S, Sharifi S, Ahmadian E et al (2019) An update on calcium carbonate nanoparticles as cancer drug/gene delivery system. *Expert Opin Drug Deliv* 16(4):331–345. https://doi.org/10.1080/17425247.2019.1587408
59. Akhmetova DR, Mitusova KA, Postovalova AS et al (2024) Size-dependent therapeutic efficiency of ^{223}Ra-labeled calcium carbonate carriers for internal radionuclide therapy of breast cancer. *Biomater Sci* 12(2):453–467. https://doi.org/10.1039/d3bm01651j
60. Karpov TE, Darwish A, Mitusova K et al (2024) Controllable synthesis of barium carbonate nano- and microparticles for SPECT and CT imaging. *J Mater Chem B* 12(17):4232–4247. https://doi.org/10.1039/d3tb02480f